

ABSTRACT

Title of dissertation: MEASURING TOPOLOGY OF BECS
IN A SYNTHETIC DIMENSIONAL LATTICE

Dina Genkina
Doctor of Philosophy, 2019

Dissertation directed by: Professor Ian Spielman
Joint Quantum Institute,
National Institute of Standards and Technology,
and
Department of Physics, University of Maryland

We describe several experiments performed on a two species apparatus capable of producing Bose-Einstein condensates (BECs) of ^{87}Rb and degenerate Fermi gases (DFGs) of ^{40}K .

We first describe computational results for observed optical depths with absorption imaging, in a regime where imaging times are long enough that recoil-induced detuning introduces significant corrections. We report that the observed optical depth depends negligibly on the cloud shape. We also find that the signal-to-noise(SNR) ratio for low atom numbers can be significantly improved by entering this regime and applying the appropriate corrections. We take advantage of this SNR improvement in our subsequent experiment colliding two clouds of ^{40}K for different values of background magnetic field in the vicinity of a Feshbach resonance. We directly imaged the fraction of scattered atoms, which was low and difficult to detect. We used this method to measure the resonance location to be $B_0 = 202.06(15)$

Gauss with width $\Delta = 10.(5)$ Gauss, in good agreement with accepted values.

Next, we describe experiments creating an elongated effectively 2D lattice for a BEC of ^{87}Rb with non-trivial topological structure using the technique of synthetic dimensions. We set up the lattice by applying a 1D optical lattice to the atoms along one direction, and treating the internal spin states of the atoms as lattice sites in the other direction. This synthetic direction is therefore very short, creating a strip geometry. We then induce tunneling along the synthetic direction via Raman coupling, adding a phase term to the tunneling coefficient. This creates an effective magnetic flux through each lattice plaquette, in the Hofstadter regime, where the flux is of order the flux quantum h/e . We detect the resulting eigenstate structure, and observe chiral currents when atom are loaded into the central synthetic site. We further launch analogues of edge magnetoplasmons and image the resulting skipping orbits along each edge of the strip.

We then applied a force along the real dimension of the 2D lattice and directly imaged the resulting motion in the transverse, synthetic, direction. We performed these measurements with 3 and 5-site width lattices along the synthetic direction. We used these measurements to identify the value of the Chern number, the topological invariant in 2D, by leveraging the Diophantine equation derived by Thouless, Kohomoto, Nightingale, and den Nijs. We measure Chern numbers with typical uncertainty of 5%, and show that although band topology is only properly defined in infinite systems, its signatures are striking even in extremely narrow systems.

Measuring topology of BECs in a synthetic dimensions lattice

by

Dina Genkina

Dissertation submitted to the Faculty of the Graduate School of the
University of Maryland, College Park in partial fulfillment
of the requirements for the degree of
Doctor of Philosophy
2019

Advisory Committee:

Professor Ian Spielman, Chair/Advisor

Professor Mohammad Hafezi, Dean's representative

Professor Steven Rolston

Professor Trey Porto

Professor Christopher Lobb

© Copyright by
Dina Genkina
2019

Acknowledgments

This thesis describes work that was carried out by many people, in a way that the multitude of authors on each of the papers only begins to convey. However, as this is the acknowledgement section of *my* thesis, I will endeavor to thank all the people that guided and supported me during my admittedly long tenure as a graduate student.

I would first and foremost like to thank my adviser, Dr. Ian Spielman, for taking a chance on a lab-averse recovering theorist. Ian's mentorship style was always patient and supportive, but without compromising on standards. Ian would never ask 'why isn't this done?', but instead ask 'how are things going this fine morning?' and offer insight and advice regarding whatever I happened to be working on. He was a role model to aspire to, both in his unique combination of intuition and rigor in physics and his unparalleled coffee consumption.

The first 'trial' semester of my lab work was spent in the RbLi lab at UMD. During that time, I am grateful to have learned from Dan Campbell, who voluntarily took on teaching me about the BEC production process one step every day, and Ryan Price, whose magical skills with all equipment and dark humor got me through that time. When I first joined the NIST lab, I had the great fortune of learning from a team of outstanding postdocs—the 'old guard'—consisting of Lindsey LeBlanc, Ross Williams, and Matthew Beeler. I thank them for an excellent introduction to not only laboratory techniques and the physics under study but also the art of working as a team.

An unparalleled debt of gratitude goes to Lauren Aycock, who shared the lab with me from day one and taught me most of what I know being an experimentalist. She endured my clumsiness and obstinance and continued teaching and supporting me throughout my time at NIST. Beyond the lab, she helped teach me how to drive and pushed me to do my first half-marathon. I cannot imagine what my graduate career would have been like without her. I would also like to thank post-docs Ben Stuhl and Hsin-I Lu for the role they played in my physics training. Ben's enthusiasm for electronic design was infectious and it was an honor to learn from him, be it about feedback loops or version control. Hsin-I's unparalleled productivity in her own work didn't stop her from taking lots of time to help me in mine. Her wisdom for knowing what the root of a problem is and how to prioritize tasks was invaluable, and she remains a role model for me today.

I am happy to have had the opportunity to work with several visiting German students: Marcell Gall, Max Schemmer, and Martin Link. Marcell excelled in balancing hard, productive work in the lab with fun in his free time, and was generally a joy to be around. Max jumped into the research with a running start, and it was exciting to see what he accomplished in a short amount of time. Martin (Marcell III) forced me to give up my belief that all crossfitters are annoying. It was a pleasure to work with him as well as to exercise and hang out with him.

My later years in the lab were spent with post-doc Mingwu Lu and fellow grad student Alina Escalera. Mingwu has taught me so much about physics, electronics, western philosophy and wine. I am grateful for having the opportunity to learn from him and get to know him. It has been a pleasure to watch Alina grow in the lab,

and to have her understanding support during the rougher parts of paper and thesis writing. Her tenacity and drive are to be admired. I have had few opportunities to spend time with new lab recruits, post-doc Amilson Fritsch and graduate student Graham Reid, but even from our limited interactions I am confident the lab will be left in good hands.

During the writing of this thesis, I have had amazing help and support from my roommates, fellow students and friends. I would like to thank Ana Valdes-Curiel, Paco Salces-Carcoba, Chris Billington, Kristen Voigt and Jon Hoffman for bravely reading through entire chapters of my thesis when I couldn't bare to even look at it. I am extremely grateful to have been part of the amazing living community that is the international house of physicists (IHOP)—it has felt more like a large family than a housing arrangement. I would like to thank both the current IHOPers, Ana, Paco, Chris and Daniel, and notable past IHOPers, Dimitry Trypogeorgos and Rory Speirs. A special thank you to Ana and Paco for unpromptedly feeding me during the final thesis writing days and to them and Chris for continued moral support. Extra special thank you to Kristen, my oldest graduate school friend, for teaching me how to drive, housing me in my times of need, providing me with thesis writing space and support, feeding me uncountable times, and telling me its okay to take a nap.

I would also like to thank Jenna Beckwith for her help at the beginning of my graduate journey, Taylor Cole for her insightful support in the last year that has allowed me to work on my thesis almost without panic, and Dr. Diane Stabler for her constant presence and support throughout my time here and for offering

deceptively simple advice. I would also like to thank the good people at Eli Lily and Company without whose pioneering research my work would not have been possible.

Above all I would like to thank my family. If it wasn't for my parents' upbringing, graduate school would never have been a possibility for me. I am grateful to them for teaching me all that they have, supporting me throughout my time as a graduate student, but prioritizing my happiness above graduate success. I would like to thank them, my sister Alya, and my brother Pten, for everything.

Table of Contents

Acknowledgements	ii
List of Tables	vii
List of Figures	viii
2 Atom–Light Interactions	1
2.1 Level structure of alkali atoms	1
2.1.1 Fine and hyperfine structure	2
2.1.2 Interaction with static magnetic fields	6
2.2 Near-resonant atom–light interaction	9
2.2.1 Rabi oscillations	9
2.2.2 Scattering	12
2.2.3 Adiabatic rapid passage	13
2.3 Far-off-resonant atom–light interaction	15
2.4 Absorption imaging	16
2.4.1 Time-of-flight and in situ imaging	19
2.5 One-dimensional optical lattices	20
2.5.1 Lattice Hamiltonian	20
2.5.2 Tight-binding approximation	24
2.5.3 Pulsing vs adiabatic loading of the lattice	25
2.6 Raman and rf coupling	29
2.6.1 Rf coupling Hamiltonian	29
2.6.2 Raman coupling Hamiltonian	32
2.6.3 Calibration of Raman and rf dressed states	37
Bibliography	41

List of Tables

List of Figures

1	Atomic structure of the ground and first excites states	4
2	Energy structure of hyperfine states of ^{87}Rb and ^{40}K	8
3	Adiabatic rapid passage (ARP)	14
4	Absorption imaging	17
5	Lattice band structure in the extended zone scheme	23
6	Lattice pulsing	27
7	Lattice pulsing for calibration	28
8	Adiabatic lattice loading	30
9	Raman and rf coupling schematic	31
10	Band structure of the rf Hamiltonian	33
11	Band structure of the Raman Hamiltonian	36
12	Pulsing on rf coupling	38
13	Pulsing on Raman coupling	40

Chapter 2: Atom–Light Interactions

In this chapter, we review the physics of interactions between atoms and light in so far as they are relevant to our experiments. We describe the level structure of alkali atoms in section 2.1, including the fine and hyperfine interactions and the effects of external magnetic fields. We review the interaction of atoms with near-resonant light (section 2.2), pertinent to cooling and absorption imaging as well as Raman and rf coupling. We then detail interactions of atoms with far-detuned light (section 2.3), pertinent to optical trapping and lattices.

In the following sections, we use these basic interactions to explain the tools used in our experiments. We describe absorption imaging (section 2.4), our detection scheme. We explain the basic physics of atoms in a 1D optical lattice potential (section 2.5), and the physics of Raman and rf coupling of hyperfine atomic levels (section 2.6).

2.1 Level structure of alkali atoms

Alkali atoms (those in the first column of the periodic table) are the most commonly used for laser cooling. Their level structure can be understood as primarily the energy state of the single electron in the outer shell, interacting with the rest of the atom—the nucleus and all the other electrons—as a whole. The quantum numbers that describe the energy levels of the atom are the principal quantum number N , that electron’s spin S , the orbital angular momentum L , and finally the nuclear spin I . The work described in this thesis was done with alkali species ^{87}Rb and ^{40}K .

2.1.1 Fine and hyperfine sturcutre

The fine structure of alkali atom comes from two corrections to the bare Hamiltonian. The bare Hamiltonian H_0 encompasses the kinetic energy and the Coulomb interaction between the outermost electron and the rest of the atom. The first of these corrections is due to special relativity—it's the correction to the classical kinetic term. The energy shift due to this term, to leading order in the small parameter of velocity over the speed of light v/c , is given by [?]

$$\Delta E_{\text{rel}} = -\frac{E_N^2}{2mc^2} \left(\frac{4N}{L - 1/2} - 3 \right), \quad (2.1)$$

where E_N is the unperturbed energy and m is the mass of the electron.

The second correction comes from the spin–orbit interaction. In the frame of the outermost electron, the nucleus is orbiting it, creating a magnetic field. The magnetic dipole moment of the electron—given by $\vec{\mu}_S = -g_S \mu_B \hat{\vec{S}}/\hbar$, where g_S is the spin g-factor, μ_B is the Bohr magneton, and $\hat{\vec{S}}$ is the spin angular momentum operator—interacts with this magnetic field. The Hamiltonian describing this interaction is given by [?, ?]

$$H_{\text{SO}} = \frac{Ze^2}{4\pi\epsilon_0} \frac{g_s}{4me^2c^2} \frac{\hat{\vec{L}} \cdot \hat{\vec{S}}}{r^3}, \quad (2.2)$$

where Z is a factor expressing the effective charge seen by the electron, e is the electron charge, ϵ_0 is the vacuum permittivity and r is the radial coordinate. This Hamiltonian does not commute with either $\hat{\vec{S}}$ or $\hat{\vec{L}}$, and therefore the projection quantum numbers m_S and m_L are no longer good quantum numbers. However, the total angular momentum $\hat{\vec{J}} = \hat{\vec{L}} + \hat{\vec{S}}$ does commute with the Hamiltonian, and therefore m_J is still a good quantum number. We can rewrite the coupling term in the spin–orbit Hamiltonian as $\hat{\vec{L}} \cdot \hat{\vec{S}} = \hat{\vec{J}}^2 - \hat{\vec{L}}^2 - \hat{\vec{S}}^2$. The leading order shift in

perturbation theory due to this interaction is given by

$$\Delta E_{\text{SO}} = \frac{E_N^2}{mc^2} \left(\frac{N[J(J+1) - L(L+1) - S(S+1)]}{L(L+1/2)(L+1)} \right). \quad (2.3)$$

Note that the relativistic and spin-orbit correction terms are of the same order. We therefore combine them into a total energy shift, called the fine structure shift. Using the fact that $S = 1/2$ and $J = L \pm 1/2$, this term can be written as

$$\Delta E_{\text{fs}} = \frac{E_N^2}{mc^2} \left(3 - \frac{4N}{J+1/2} \right), \quad (2.4)$$

which splits the atomic energies according to the quantum number J .

The ground state of ^{87}Rb , in term notation $N^{2S+1}L_J$ is $5^2s_{1/2}$, where s is orbital notation indicating $L = 0$. Since $L = 0$, the ground state only has one possible value of $J = 1/2$, and there is no ground state fine structure splitting. The first excited state 5^2p_J has orbital angular momentum $L = 1$ (as indicated by p in orbital notation). Therefore, J can take on two different values: $1/2$ and $3/2$, producing a hyperfine splitting between the $5^2p_{1/2}$ and $5^2p_{3/2}$. The spectral feature associated with the ground $5^2s_{1/2}$ and lower excited $5^2p_{1/2}$ energy difference is conventionally called the $D1$ line, and the feature corresponding to the splitting between $5^2s_{1/2}$ and $5^2p_{3/2}$ is the $D2$ line. For other alkalis, including ^{40}K , the ground state values of L and S are identical and only the N value is different. Therefore, even though their energies vary, $D1$ and $D2$ lines feature in all alkalis.

There is a yet smaller correction to the bare Hamiltonian, causing what's known as the hyperfine splitting. This arises from the interaction of the nuclear spin magnetic dipole moment with the magnetic field created by the electron. The Hamiltonian for this interaction is

$$H_{\text{hfs}} = -\hat{\vec{\mu}}_I \cdot \vec{B}, \quad (2.5)$$

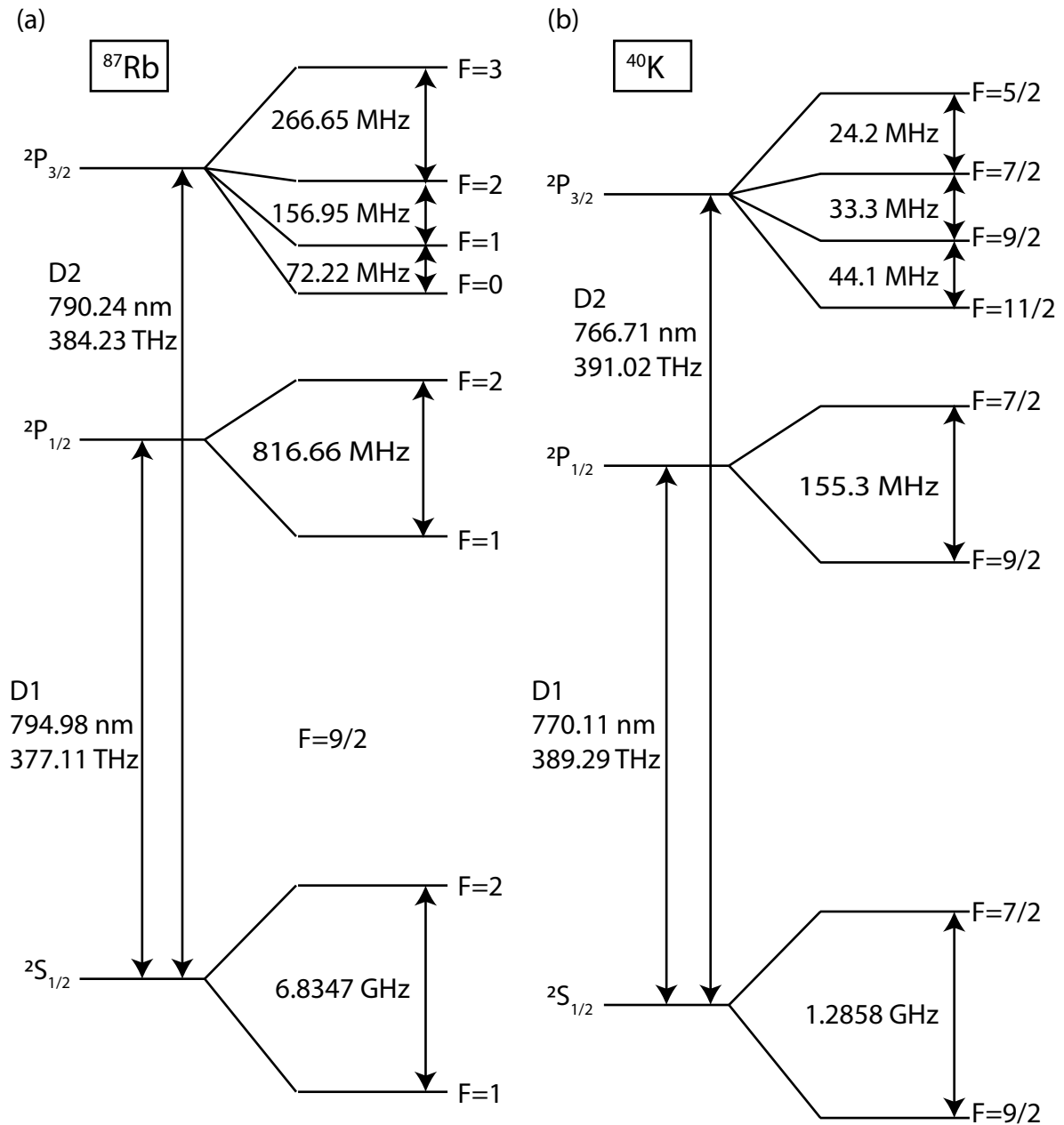


Figure 1: Atomic structure of the ground and first excites states, with fine and hyperfine splittings. (a) ^{87}Rb . Values from [?]. (b). ^{40}K . Values from [?].

where $\hat{\mu}_I = g_I \mu_B \hat{I}$ is the nuclear spin magnetic dipole moment, \hat{I} is the nuclear spin operator and \vec{B} is the magnetic field seen by the nucleus. The nuclear spin g-factor g_I encompasses the entire complex structure of the nucleons, but is generally smaller than the electron spin g-factor g_S by a factor of m_e/m_p , where m_e is the electron mass and m_p is the proton mass, making this term very small. This magnetic field, to leading order, is given by [?, ?]

$$\vec{B} = 2\frac{\mu_0}{4\pi}\mu_B \left(\frac{\hat{\vec{L}}}{\hat{r}^3} - \frac{1}{\hat{r}^3} \left[\hat{\vec{S}} - 3\frac{\hat{\vec{S}} \cdot \hat{\vec{r}}}{\hat{r}^2} \hat{\vec{r}} \right] + \frac{2}{3}\delta(\vec{r})\hat{r}^2 \hat{\vec{S}} \right), \quad (2.6)$$

where the first term arises from the field due to the orbital angular momentum of the electron, the second term is the field created by the electron spin magnetic dipole moment, and the final term is the contact interaction, which is only non-zero for $L = 0$ states. The hyperfine Hamiltonian eqn. 2.5 contains both $\hat{I} \cdot \hat{L}$ and $\hat{I} \cdot \hat{S}$ terms. Therefore, \hat{L} , \hat{S} and \hat{I} as well as \hat{J} no longer commute with the Hamiltonian and projection quantum numbers m_L , m_S , m_J and m_I are no longer good quantum numbers. However, the total spin including nuclear spin $\hat{F} = \hat{L} + \hat{S} + \hat{I}$ commutes with the Hamiltonian, and total spin F and its projection m_F are now good quantum numbers.

The energy shift, to lowest order in perturbation theory, due to the hyperfine interaction is given by [?, ?]

$$\Delta E_{\text{hfs}} = \frac{1}{2}A_{\text{hfs}}K + B_{\text{hfs}} \frac{\frac{3}{2}K(K+1) - 2I(I+1)J(J+1)}{2I(2I-1)2J(2J-1)}, \quad (2.7)$$

where $K = F(F+1) - I(I+1) - J(J+1)$, A_{hfs} is the magnetic dipole constant of the electron, whose values for ^{87}Rb and ^{40}K can be found in [?, ?].

For ^{87}Rb , $I = 3/2$ and for ^{40}K , $I = 4$. The interaction with the nuclear spin splits the ground state of ^{87}Rb into two manifolds, $F = 1$ and $F = 2$. Similarly for ^{40}K , it splits the ground state into $F = 9/2$ and $F = 7/2$ manifolds. The

structure of the ground and first excited states of ^{87}Rb and ^{40}K , including both the fine and hyperfine splittings, is diagrammed in Figure 1. Note that the $D1$ and $D2$ transitions are in the optical regime, making them amenable to laser cooling. The fine structure splitting of the excited states is in the far infrared, whereas the hyperfine splitting of the ground states is in the microwave regime.

2.1.2 Interaction with static magnetic fields

In a static background magnetic field \vec{B} , the atomic angular momentum interacts with the field via the Hamiltonian

$$H_B = \frac{\mu_B}{\hbar} (g_S \hat{\vec{S}} + g_L \hat{\vec{L}} + g_I \hat{\vec{I}}) \cdot \vec{B}, \quad (2.8)$$

where μ_B is the Bohr magneton, g_S , g_L and g_I are the spin, orbital and nuclear Landé g-factors correcting their respective magnetic dipole moments. Without loss of generality, we can define the magnetic field to be in the e_z direction, $\vec{B} = B_z e_z$, to obtain

$$H_B = \frac{\mu_B}{\hbar} (g_S \hat{S}_z + g_L \hat{L}_z + g_I \hat{I}_z) B_z. \quad (2.9)$$

At very low magnetic field strengths, where the energy shift due to H_B is small compared to the hyperfine splitting, the total angular momentum F remains a good quantum number, and the Hamiltonian in eqn. 2.10 can be re-written as

$$H_B = \frac{\mu_B}{\hbar} (g_F \hat{F}_z) B_z, \quad (2.10)$$

where the effective Lande g-factor is dependent on the angular momentum quantum

numbers:

$$g_F = g_J \frac{F(F+1) - I(I+1) + J(J+1)}{2F(F+1)} + g_I \frac{F(F+1) + I(I+1) - J(J+1)}{2F(F+1)}. \quad (2.11)$$

In this regime, the levels split linearly according to the \hat{F}_z projection quantum number, m_F . For the ground state of ^{87}Rb , it splits into three hyperfine states in the $F = 1$ manifold ($m_F = 0, \pm 1$) and five hyperfine states in the $F = 2$ manifold ($m_F = 0, \pm 1, \pm 2$). This regime is at fields $B \leq \approx 1$ Gauss for ^{87}Rb , as seen in Figure 2.

At fields producing energy shifts small compared to the fine structure splitting, but large compared to the hyperfine splitting, F is no longer a good quantum number, and the relevant Hamiltonian becomes

$$H_B = \frac{\mu_B}{\hbar} (g_J \hat{J}_z + g_I \hat{I}_z) B_z. \quad (2.12)$$

Here, since $g_I \ll g_J$, the energy dependence on B_z is dominated by a linear dependence on the \hat{J}_z projection quantum number, m_J , as seen in the higher field limit in Figure 2.

In the intermediate regime, there is in general no analytic solution for the eigenenergies and one must resort to numerics. However, for the specific case of $J = 1/2$ applicable to alkali ground states, there is an analytic solution given by the Breit-Rabi formula [?]:

$$E_{|J=1/2 m_J I m_I\rangle} = -\frac{\Delta E_{\text{hfs}}}{2(2I+1)} + g_I \mu_B m B \pm \frac{\Delta E_{\text{hfs}}}{2} \left(1 + \frac{4mx}{2I+1} + x^2 \right)^{1/2}, \quad (2.13)$$

where ΔE_{hfs} is the zero field hyperfine splitting, $m = m_I \pm m_J$, and

$$x = \frac{(g_J - g_I)\mu_B B}{\Delta E_{\text{hfs}}}. \quad (2.14)$$

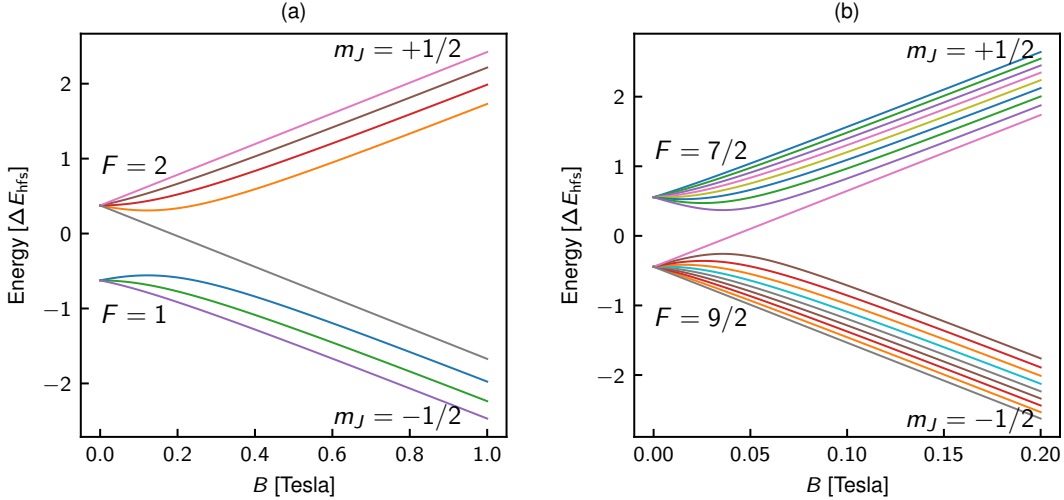


Figure 2: Energy structure of hyperfine states of the ground state of (a) ^{87}Rb and (b) ^{40}K as a function of external magnetic field strength in Gauss. Note that the zero field splitting ΔE_{hfs} by which the vertical axis is scaled is different for the two atomic species.

From this we can get a better picture of the shifts at low fields, where $\mu_{\text{B}}B \ll E_{\text{hfs}}$. Expanding eqn. 2.13 to second order in small parameter $4mx/(2I+1) + x^2$, and neglecting the field-independent terms, we obtain

$$\Delta E_{|J=1/2m_JIm_I\rangle} \approx \frac{\Delta E_{\text{hfs}}}{2} \left(\frac{1}{2} \left[\frac{4mx}{2I+1} + x^2 \right] - \frac{1}{8} \left[\frac{16m^2x^2}{(2I+1)^2} + \frac{4mx^3}{2I+1} + x^4 \right] \right). \quad (2.15)$$

We recognize the term linear in mx , $\Delta E_{\text{hfs}}mx/(2I+1) = (g_J - g_I)\mu_{\text{B}}Bm/(2I+1)$.

In addition, there is a term quadratic in mx :

$$\Delta E_{\text{hfs}} \frac{m^2x^2}{(2I+1)^2} = \frac{(g_J - g_I)^2\mu_{\text{B}}^2B^2m^2}{\Delta E_{\text{hfs}}(2I+1)^2} = \epsilon(B)m^2, \quad (2.16)$$

where in the last term we have defined $\epsilon(B)$, the magnitude of this ‘quadratic’ Zeeman energy shift. For the magnetic field strengths used in experiments described in this thesis, the linear term plus quadratic correction are sufficient for describing the energy levels.

The form of the approximate Hamiltonian in this regime for any value of F is given by

$$H_0 = H_{\text{KE}} + \hbar\omega_z \hat{F}_z + \hbar\epsilon \hat{F}_z^2, \quad (2.17)$$

where $\hbar\omega_z = \mu_B g_F B_z / \hbar$, and the kinetic energy Hamiltonian $H_{\text{KE}} = \hbar^2 \vec{k}^2 / 2m\hat{\mathcal{I}}$, and $\hat{\mathcal{I}}$ is the identity matrix.

2.2 Near-resonant atom–light interaction

In this section, we will assume the atom can be treated as a two-level system: one with a ground state of some energy $\hbar\omega_g$ and excited state with energy $\hbar\omega_e$, with an energy difference $\hbar\omega_0$. When such an atom, starting in the ground state, is illuminated by a laser beam with frequency $\hbar\omega_L$, there are three kinds of transitions that occur: during absorption the atom absorbs a photon from the laser and goes from the ground to the excited state; during stimulated emission, the atom emits a photon into the field of the laser beam and jumps from the excited to the ground state; during spontaneous emission, the atom decays to the ground state from the excited state with no help from the laser, emitting into a random vacuum mode. Stimulated emission results in coherent light co-propagating with the laser beam, while spontaneous emission results in light scattering in any direction. The rate of spontaneous emission from an excited state is given by the natural transition linewidth of the atomic transition Γ .

2.2.1 Rabi oscillations

On timescales short compared to $1/\Gamma$, spontaneous emission can be ignored, and an atom undergoes coherent Rabi oscillations between the ground and excited states via cycles of absorption and stimulated emission [?]. Let us consider the

Hamiltonian

$$H = H_0 + H_L(t), \quad (2.18)$$

where H_0 is the bare atomic Hamiltonian and H_L is the interaction with the laser beam. The interaction with the laser results from the electric dipole moment of the atom $\vec{d} = -\epsilon_0 \vec{r}$ interacting with the electric field of the beam $\vec{\mathcal{E}}(t, \vec{r})$, giving

$$H_L(t) = -\vec{d} \cdot \vec{\mathcal{E}}(t, \vec{r}). \quad (2.19)$$

We can write the wavefunction Ψ as a linear combination of the two eigenstates (for a two-level atom) of the bare Hamiltonian H_0 as

$$\Psi = c_g(t)\phi_g(\mathbf{r})e^{-i\omega_g t} + c_e(t)\phi_e(\mathbf{r})e^{-i\omega_e t}, \quad (2.20)$$

where $c_g(t)$ and $c_e(t)$ are the time-dependent coefficients multiplying the eigenstate wavefunctions ϕ_g and ϕ_e of the ground and excited state respectively, and \mathbf{r} is the spatial coordinate. Absorbing any diagonal elements of H_L into H_0 , multiplying both sides of the Schrödinger equation from the left by ψ_j and integrating over \mathbf{r} , we can write down the Schrödinger equation as two coupled equations:

$$i\hbar \frac{dc_g(t)}{dt} = c_e(t)H_L^{ge}(t)e^{-i\omega_0 t} \quad (2.21)$$

and

$$i\hbar \frac{dc_e(t)}{dt} = c_g(t)H_L^{eg}(t)e^{i\omega_0 t}, \quad (2.22)$$

where $\omega_0 = \omega_e - \omega_g$ is the transition frequency, $H_L^{ge}(t)$ is the off-diagonal element of the laser coupling Hamiltonian that couples the excited to the ground state and $H_L^{ge}(t) = H_L^{eg*}(t)$. This coupling Hamiltonian can be written in terms of the electric field produced by the laser beam coupling to the electric dipole moment of the atom

as

$$H_{\text{L}}^{ge}(t) = \hbar\Omega\cos(kz - \omega_{\text{L}}t) \quad (2.23)$$

with

$$\Omega = \frac{-e\mathcal{E}}{\hbar} \int \phi_g(\mathbf{r}) \mathbf{r} \phi_e(\mathbf{r}) d^3r \quad (2.24)$$

the Rabi frequency, characterizing the coupling strength between the laser field (with electric field amplitude \mathcal{E}) and the atom. Here, e is the charge of the electron. The Rabi frequency can also be related to the natural linewidth of the atomic transition Γ via $\Omega^2 = \frac{\Gamma\lambda_{\text{L}}^3}{h(2\pi)^3}I$, with λ_{L} as the laser wavelength, h as Plank's constant and I as the laser intensity.

To solve this Schrödinger equation, we make the traditional transformation to the rotating frame:

$$c'_g(t) = c_g(t) \quad (2.25)$$

$$c'_e(t) = c_e(t)e^{-i\delta t}, \quad (2.26)$$

where $\delta = \omega_0 - \omega_{\text{L}}$ is the detuning of laser light from resonance. In this frame, we can write the atom-light Hamiltonian in the $\begin{pmatrix} c'_g \\ c'_e \end{pmatrix}$ basis as:

$$H = \hbar \begin{pmatrix} -\delta/2 & \Omega/2 \\ \Omega/2 & \delta/2 \end{pmatrix}. \quad (2.27)$$

In the limit of no coupling, $\Omega = 0$, in the rotating frame the eigenenergies are $E_{\pm} = \pm\hbar\delta/2$. For non-zero coupling, finding the eigenvalues of H gives

$$E_{\pm} = \pm\hbar\sqrt{\delta^2 + \Omega^2}/2. \quad (2.28)$$

The eigenenergies are shifted in the presence of the light.

Assuming the atom starts in the ground state $c_g(t=0) = 1$, we can solve the time-dependent Schrödinger equation (TDSE) with the above Hamiltonian

$$i\hbar \frac{d}{dt} \begin{pmatrix} c'_g \\ c'_e \end{pmatrix} = H \begin{pmatrix} c'_g \\ c'_e \end{pmatrix} \quad (2.29)$$

we obtain the oscillating excited state amplitude

$$c'_e(t) = -i \frac{\Omega}{\sqrt{\Omega^2 + \delta^2}} \sin \left(\frac{\sqrt{\Omega^2 + \delta^2} t}{2} \right), \quad (2.30)$$

known as Rabi oscillations. The frequency of these oscillations is the generalized Rabi frequency $\Omega' = \sqrt{\Omega^2 + \delta^2}$. The amplitude of the oscillation is at its maximum when the laser is on-resonance, $\delta = 0$. As the detuning increases, the contrast in excited and ground populations decreases, while the frequency of the oscillation increases.

2.2.2 Scattering

In the regime where spontaneous emission cannot be ignored, Rabi oscillations of each individual atom are intermittently interrupted by decay to the ground state. Averaging over an atomic ensemble, on the time scale of a single Rabi oscillation, the overall excited state population reaches a steady state, and the rate of spontaneous emission becomes constant. Since during spontaneous emission the ejected photon can go into any vacuum mode, this process can be thought of as the scattering of photons by the atoms. This scattering rate is given by [?]

$$\gamma_{sc} = \frac{\Gamma}{2} \frac{I/I_{sat}}{1 + 4(\delta/\Gamma)^2 + I/I_{sat}}, \quad (2.31)$$

where I_{sat} is the saturation intensity. This is the intensity at which the timescale of spontaneous emission matches the Rabi oscillation rate, reducing the capacity for absorption of extra light.

2.2.3 Adiabatic rapid passage

Suppose there is a two-level atom in its ground state that an experimenter wants to transfer into the excited state. To transfer it with perfect fidelity using Rabi oscillations, one would need a perfectly on-resonant beam and very precise timing to shut off the coupling field at the maximum of the excited state population. This is challenging and not very stable to small perturbations in the level splitting between the ground and excited state (caused by small field fluctuations for the case of two Zeeman sublevels). A more robust technique is known as adiabatic rapid passage.

Suppose the two energy levels of the atom are sensitive to some external parameter. Commonly (as in the case of hyperfine sublevels), they are sensitive to an external magnetic field B , and in the small field limit are linear in B . Therefore, the detuning that goes into the Hamiltonian in eqn. 2.27 becomes $\hbar\delta = AB - \hbar\omega_L$, where A is the coupling constant in the hyperfine (or other) Hamiltonian. In the limit of zero coupling strength, diagonalizing the Hamiltonian amounts to calculating the eigenenergies in the rotating frame as a function of the control parameter B . These are represented in black in Figure 3. Note that the two levels cross each other when their energy difference matches $\hbar\omega_L$, on resonance.

Once the coupling field is turned on (in the case of the hyperfine interaction, and rf-field), the two levels split near the resonance and an avoided crossing appears, as seen in blue in Figure 3. Crucially, away from resonance towards the left, the bottom coupled state overlaps closely with the uncoupled (black state). Far from resonance, the ground state is largely unaffected by the presence of light. On the other hand, far from the resonance on the right, the lower coupled state overlaps

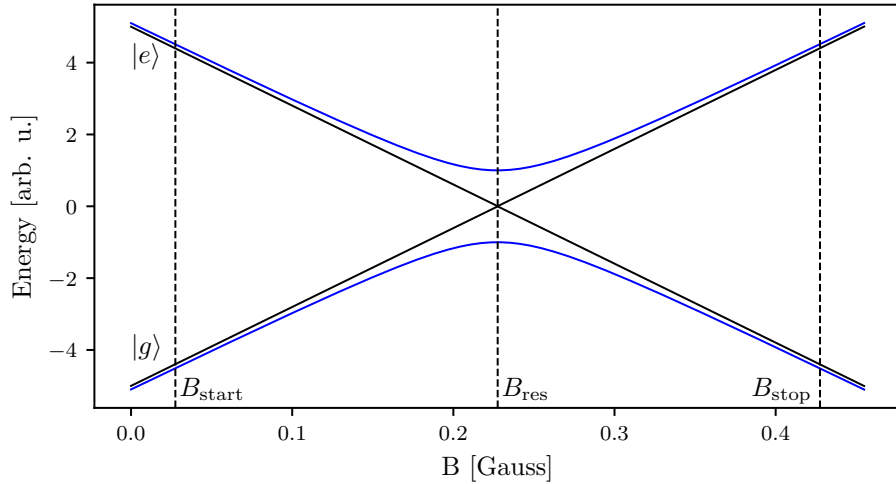


Figure 3: Adiabatic rapid passage (ARP). Black lines represent energies of the ground and excited state, in the rotating frame, with zero coupling. Blue lines represent these bands with some coupling $\hbar\Omega$ turned on. The dashed lines represent the starting point of an ARP (B_{start}), the resonant field value (B_{res}) and the end point of an ARP (B_{stop}).

almost perfectly with the excited uncoupled state. Adiabatic rapid passage (ARP) takes advantage of this change.

The ARP protocol is as follows. Start at a bias field (or other control parameter) where turning on the coupling field does not significantly perturb the eigenstate (B_{start} in the figure). Turn on the coupling field adiabatically (slow with respect to the time scale associated with the level splitting energy at the selected detuning $\tau = \hbar/(E_e - E_g)$), such that the atom remains entirely in the ground state $|g\rangle$. Then, sweep the control parameter across the resonance, again adiabatically with respect to the coupled level splitting (blue in the figure). The sweep rate can be optimized to be faster away from resonance, where $E_e - E_g$ is large and slower closer to the avoided crossing. Then, at a final value of the control parameter where the lowest coupled state overlaps almost perfectly with the bare excited state $|e\rangle$, adiabatically turn off the coupling field, leaving the atoms in the excited state.

The ‘rapid’ part of adiabatic rapid passage refers to the procedure having to

be fast with respect to the spontaneous emission timescale, since in the coupled basis there is some population in the excited state and spontaneous decay would disrupt the process. This procedure is relatively insensitive to field fluctuations (as long as B_{res} is roughly in the middle of the relatively long sweep, the procedure will succeed). It can also be applied to multi-level situations, for example in the case of the hyperfine states of a single manifold F , where the atoms traverse multiple avoided crossings in the same sweep and can be efficiently transferred from one stretch state $m_F = F$ to the other $m_F = -F$, or vice versa.

2.3 Far-off-resonant atom–light interaction

We can infer the behavior of atoms in a far-detuned laser field by taking the solutions from eqns. 2.28 and 2.30 in the limit $\delta \gg \Omega$. First, looking at the excited state population in eqn. 2.30, the amplitude of the excited state population oscillation approaches zero. Therefore, as expected, no absorption of the light actually takes place and the atom remains in the ground state. However, the light still affects the atom by shifting the eigenenergies via eqn. 2.28. Recalling that the bare eigenenergies in the rotating frame are given by $E_{\pm} = \pm\hbar\delta/2$, the energy shift from bare is given by

$$\Delta E_{\pm} = \pm\hbar\sqrt{\delta^2 + \Omega^2}/2 - \pm\hbar\delta/2. \quad (2.32)$$

Expanding the energy shift in the small parameter Ω/δ , we obtain the shifted energies $E_{\pm} = \pm\hbar\sqrt{\delta^2 + \Omega^2}/2 \approx \pm(\delta/2 + \Omega^2/4\delta)$. The shift from bare energy levels is thus

$$\Delta E_{\pm} \approx \pm\hbar(\delta/2 + \Omega^2/4\delta) - \pm\hbar\delta/2 = \pm\hbar\Omega^2/4\delta. \quad (2.33)$$

This laser-intensity-dependent energy shift is called the AC Stark shift, and is the basis of most laser created potentials for cold atoms.

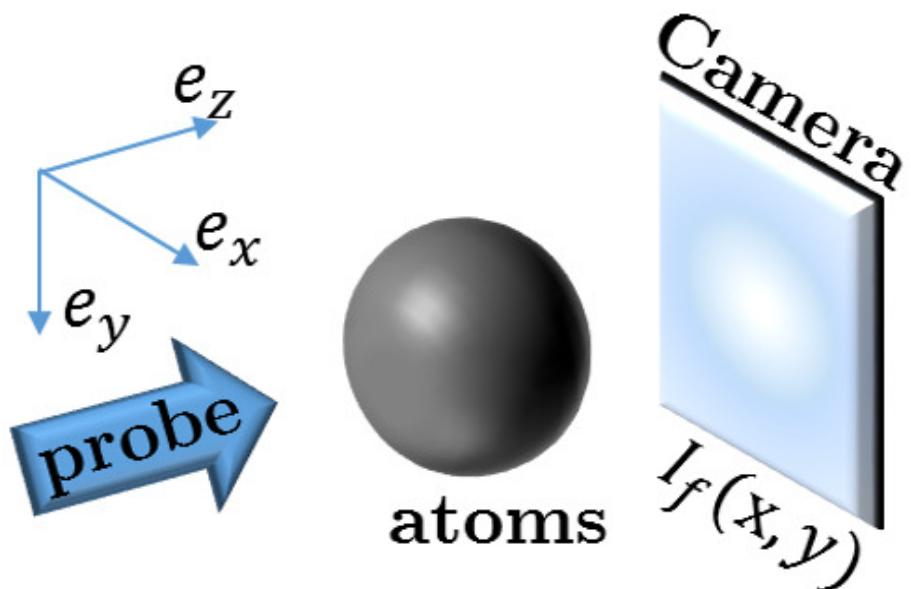
For the ground state, and a red detuned laser beam (where the laser frequency

is lower than the resonant frequency), this creates energy minima in locations of maximal laser intensity. For the lattice described in this chapter, as well as for the trapping of our atoms in the final stages of cooling, we use high power (up to 10 W) lasers with wavelength $\lambda_L = 1064$ nm.

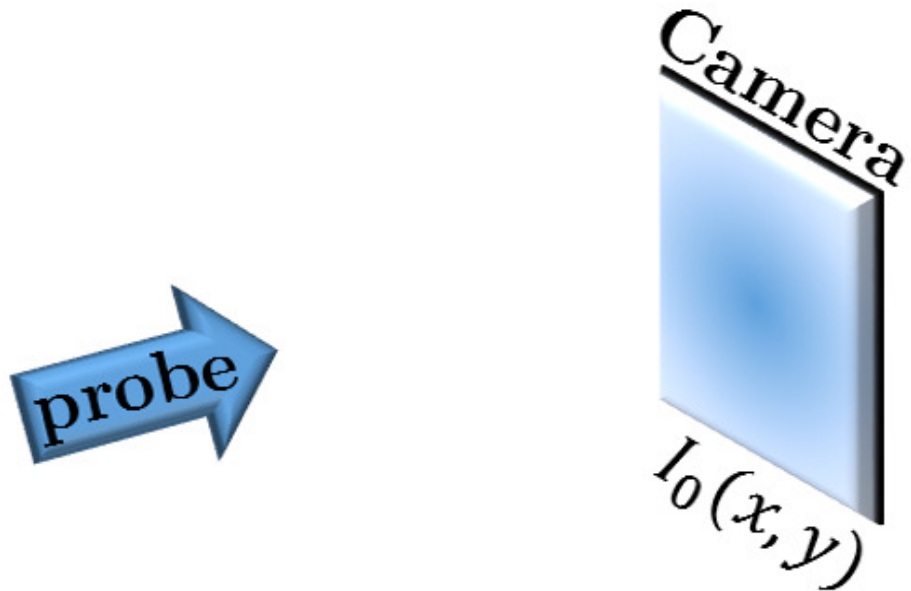
2.4 Absorption imaging

Absorption imaging takes advantage of the on-resonant interaction described in the previous section. An on or near-resonant laser beam ($\delta/\Gamma \ll 1$) is shined at the atoms, and the absorbed light acts to create a shadow in the shape of the atoms in the laser beam. This beam with the shadow is then imaged on a camera, in our case a CCD, as depicted in Figure 4a (top). This is called the atom image, and the intensity distribution over the camera is denoted by $I_f(x, y)$, where the subscript f stands for final - the intensity after the light has encountered the atoms. To quantify the ‘shadowed out’ intensity, after the atoms have left the trap, the same laser intensity is shined directly at the camera, as in Figure 4a (bottom). This is called the probe image, and the intensity distribution over the camera is denoted by $I_0(x, y)$, where the subscript 0 indicated initial—the intensity before the light had encountered the atoms.

To recover the atom number distribution encountered by the light, consider an atomic cloud with 3D density $\rho(x, y, z)$. Since we can only obtain 2D information from the camera, we can only hope to recover a 2D atomic column density $n(x, y) = \int \rho(x, y, z) dz$. Focusing in on a single pixel of the camera, we can consider a single value of I_0 and I_f to recover a local n . As the laser light propagates through the atomic cloud, the intensity of the light will diminish due to absorption. This absorption as a function of propagation direction z can be expressed using the scattering rate equation eqn. 2.31 as the number of photons scattered by the atoms (proportional to the atomic density times the scattering rate) times the photon



Imaging with atoms



Imaging without atoms

(a)

energy $\hbar\omega_L$:

$$\frac{d}{dz} \frac{I(z)}{I_{\text{sat}}} = -\hbar\omega_L \rho(z) \gamma_{sc}(z) = -\rho(z) \sigma_0 \frac{I(z)/I_{\text{sat}}}{1 + 4\delta^2/\Gamma^2 + I(z)/I_{\text{sat}}}, \quad (2.34)$$

where the resonant scattering cross section is $\sigma_0 = 3\lambda_0^2/2\pi$, and λ_0 is the wavelength associated with atomic resonance.

Integrating both sides of eqn. 2.34, we obtain

$$\sigma_0 n = (1 + 4\delta^2/\Gamma^2) \ln(I_0/I_f) + (I_0 - I_f)/I_{\text{sat}}. \quad (2.35)$$

The quantity $\text{OD} = \ln(I_0/I_f)$ is called the optical depth of the cloud. When the probe intensity I_0 is much smaller than the saturation intensity, the second term in eqn. 2.35 becomes negligible. Assuming further that the probe light is on resonance, $\delta = 0$, the atomic column density becomes simply $\sigma_0 n = \text{OD}$. Figure 4b shows a Gaussian atomic density distribution (top) and the resulting probe intensity as a function of position in the cloud (bottom). The intensity drops from its initial to final value gradually as it traverses the cloud.

However, there is an important effect that the above equations do not account for. Namely, as the atoms absorb light from the probe beam, they also get a momentum kick equal to the momentum of a photon during each collision $\hbar k_r = h/\lambda_L$ in the direction of propagation. It is true that the absorbed photon will then be re-emitted by the atom, inducing a loss of momentum, but since this happens through the process of spontaneous emission into a random vacuum mode, the average momentum kick acquired this way over many re-emissions will average to zero. On average, each photon absorbed will induce a change in velocity of the atom of $v_r = \hbar k_r/m$, where m is the atomic mass, as depicted in Fig. 4c. As the velocity of the atom changes, due to the Doppler effect, the apparent laser frequency will change as well. Therefore, even if the laser light is exactly on-resonant for a stationary atom, it

will become off-resonant for longer imaging times, and eqn. 2.34 will acquire a time dependence. For most experiments, this effect is small and can be neglected. However, if the imaging time becomes of order a recoil time t_r , a time after which the recoil-induced detuning δ becomes of order Γ , this effect becomes significant. We explore this effect in Chapter ??.

2.4.1 Time-of-flight and in situ imaging

There are two commonly used protocols for measuring cold atomic clouds, in situ and time-of-flight measurements. Generally, the atomic cloud is trapped (in our case by an optical dipole trap) during the experiment. In situ is Latin for in its original place. As suggested by the name, in situ measurements are taken while the cloud is still in its original trap, or immediately after the trap is turned off before any dynamics have had time to occur. These measurements measure the real spatial distribution of the atoms at the end of the given experiment. There is a difficulty associated with making in situ measurements of BECs, however. Namely, BECs in their original trap tend to be relatively dense, with optical depths often in excess of $OD \approx 20$, requiring unrealistic probe light intensities to resolve. One way to bypass this difficulty is to selectively image only a small fraction of the condensed atoms, as was done with microwave imaging for our magnetic field stabilization feed-forward protocol. Another option is to instead perform a time-of-flight measurement, which reduce the density of the cloud but don't give access to the original density distribution.

In time-of-flight measurements, the trapping potential is abruptly snapped off after the experiment, and the atoms are allowed to free fall and expand for some time t . For our experiments, t was on the order of tens of milliseconds. In the regime where time t is long enough that the atoms travel much further than the initial extent of the cloud in the directions transverse to the imaging axis, the final

position of the atoms is determined almost exclusively by their in situ momentum, not their in situ position. Therefore, time-of-flight imaging in this regime measures the atomic distribution as a function of momentum, not position.

2.5 One-dimensional optical lattices

2.5.1 Lattice Hamiltonian

Our 1-D optical lattice is created by retro-reflecting the $\lambda_L = 1064$ nm laser, creating a standing wave of light. Via the AC Stark shift, this creates a periodic potential for the atoms of the form

$$V = -V_0 \sin^2(k_L x), \quad (2.36)$$

where $k_L = 2\pi/\lambda_L$ is the wavenumber associated with the lattice recoil momentum. The time-independent Hamiltonian, for some eigenenergy E_n , will be given by

$$-\frac{\hbar^2}{2m} \frac{d^2}{dx^2} \Psi_n(x) - V_0 \sin^2(k_L x) \Psi_n(x) = E_n \Psi_n(x). \quad (2.37)$$

Since the potential is spatially periodic, we can invoke Bloch's theorem [?]:

$$\Psi_{n,q} = e^{iqx} u_{n,q}(x), \quad (2.38)$$

where q is the crystal momentum restricted to $\pm\hbar k_L$, and $u_{n,q}(x)$ is the spatially-varying part of the wavefunction obeying the spatial periodicity of the lattice. Plugging this in to the Hamiltonian, we obtain

$$-\frac{\hbar^2}{2m} \left(-q^2 + 2iq \frac{d}{dx} + \frac{d^2}{dx^2} \right) u_{n,q}(x) - V_0 \sin^2(k_L x) u_{n,q}(x) = E_n u_{n,q}(x). \quad (2.39)$$

Expanding $u_{n,q}(x)$ in Fourier components commensurate with the lattice period of $2k_L$ as $u_{n,q}(x) = \sum_{j=-\infty}^{\infty} a_j e^{i2k_L j x}$, we obtain

$$\sum_j \left(\frac{\hbar^2}{2m} (q + 2k_L)^2 a_j - V_0 \sin^2(k_L x) a_j \right) e^{i2k_L j x} = E_n \sum_j a_j e^{i2k_L j x}. \quad (2.40)$$

Re-writing $\sin^2(k_L x) = (e^{-2ik_L x} + e^{2ik_L x} - 2)/4$, multiplying both sides by $e^{i2k_L j' x}$ and invoking $\sum c_j e^{ik(j-j')} = \delta_{jj'}$, where $\delta_{jj'}$ is the Kroniker delta and c_j are appropriately normalized coefficients, we get for any value of the index j

$$\frac{\hbar^2}{2m} (q + 2k_L j)^2 a_j - \frac{V_0}{4} (a_{j+1} + a_{j-1}) = E_n a_j. \quad (2.41)$$

This can be expressed in matrix form

$$H_L = \begin{pmatrix} \ddots & & & & & \\ & \frac{\hbar^2}{2m} (q + 4k_L)^2 & -\frac{V_0}{4} & 0 & 0 & 0 \\ & -\frac{V_0}{4} & \frac{\hbar^2}{2m} (q + 2k_L)^2 & -\frac{V_0}{4} & 0 & 0 \\ & 0 & -\frac{V_0}{4} & \frac{\hbar^2}{2m} q^2 & -\frac{V_0}{4} & 0 \\ & 0 & 0 & -\frac{V_0}{4} & \frac{\hbar^2}{2m} (q - 2k_L)^2 & -\frac{V_0}{4} \\ & & 0 & 0 & -\frac{V_0}{4} & \frac{\hbar^2}{2m} (q - 4k_L)^2 \\ & & & & & \ddots \end{pmatrix}, \quad (2.42)$$

in the basis of momentum orders $|k\rangle = e^{ikx}$ given by:

$$\begin{pmatrix} \vdots \\ |q + 4k_L\rangle \\ |q + 2k_L\rangle \\ |q\rangle \\ |q - 2k_L\rangle \\ |q - 4k_L\rangle \\ \vdots \end{pmatrix}. \quad (2.43)$$

This matrix can be diagonalized for every value of the crystal momentum q , with the resulting band structure shown in Figure 5. It is convenient to define the lattice recoil energy $E_L = \hbar^2 k_L^2 / 2m$. Then, we can re-write the Hamiltonian with V_0 in units of E_L and momenta q in units of k_L as

$$H_L/E_L = \begin{pmatrix} \ddots & & & & & \\ & (q+4)^2 & -\frac{V_0}{4} & 0 & 0 & 0 \\ & -\frac{V_0}{4} & (q+2)^2 & -\frac{V_0}{4} & 0 & 0 \\ & 0 & -\frac{V_0}{4} & q^2 & -\frac{V_0}{4} & 0 \\ & 0 & 0 & -\frac{V_0}{4} & (q-2)^2 & -\frac{V_0}{4} \\ & 0 & 0 & -\frac{V_0}{4} & (q-4)^2 & \ddots \end{pmatrix}. \quad (2.44)$$

In any numerical simulation, the number of momentum orders that can be included is finite. We determine the value of the parameter $n = \max(|j|)$ as the lowest n at which the eigenvalues stop changing to machine precision from $n-1$.

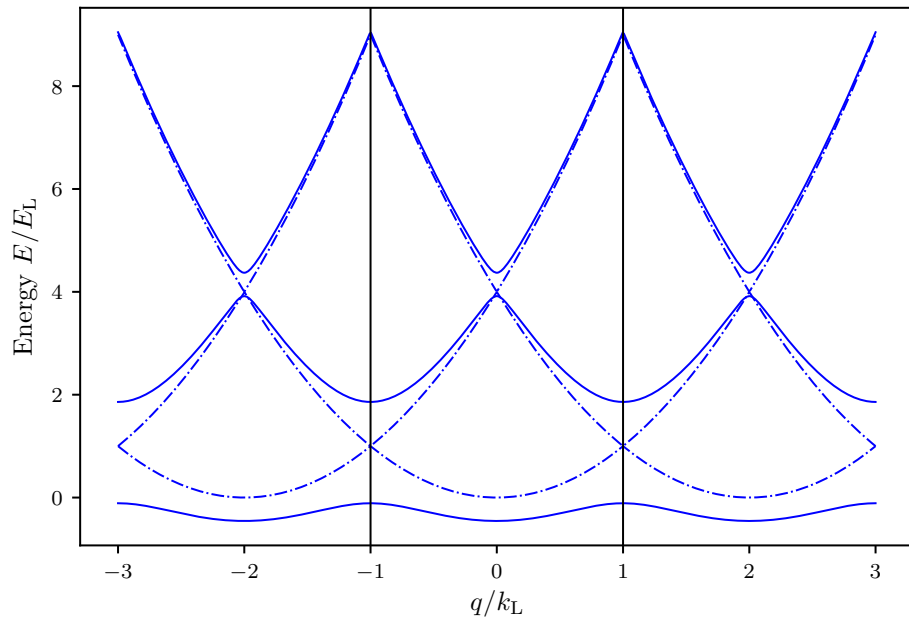


Figure 5: Lattice band structure in the extended zone scheme. The dashed lines represent the limit of zero lattice depth, with the regular parabolic dispersion relation of a free particle repeating with the reciprocal lattice period. The solid lines are the dispersion relation at $V_0 = 4.0E_L$, showing the opening of gaps at crossings of the zero lattice depth bands. The black lines demarcate the first Brillouin zone.

2.5.2 Tight-binding approximation

In the limit of large lattice depths, $V_0 > \approx 5E_L$, the lattice Hamiltonian is well approximated by the tight-binding model with only nearest neighbor hopping. In the tight-binding model, the basis is assumed to be a set of orthogonal functions, called Wannier functions, localized to each lattice site $|j\rangle$. The approximation lies in assuming only nearest neighbor tunnelings between the sites, forming the nearest-neighbor tight-binding Hamiltonian

$$H_{\text{tb}} = -t |j\rangle \langle j+1| + \text{H.c.}, \quad (2.45)$$

where t is the tunneling amplitude between nearest neighbor sites and H.c. stands for Hermitian conjugate. We have neglected the diagonal energy term, as it will be equal for every Wannier function $|j\rangle$ and thus represents a constant energy offset. All the information about the lattice depth is therefore reflected in the tunneling amplitude t .

This Hamiltonian can also be expressed in the momentum basis by Fourier transforming the basis functions:

$$|j\rangle = \frac{1}{\sqrt{N}} \sum_{k_j} e^{-ik_j j} |k_j\rangle, \quad (2.46)$$

giving the Hamiltonian

$$H_{\text{tb}} = -\frac{1}{N} \sum_{k_1} \sum_{k_2} t e^{-ijk_1} e^{ik_2(j+1)} |k_1\rangle \langle k_2| + \text{H.c.} = - \sum_k 2t \cos(k) |k\rangle \langle k|. \quad (2.47)$$

From this we can directly read off the band structure of the tight binding Hamiltonian. First, we notice that we only obtain one band—to approximate higher bands with the tight-binding approximation we would need to construct a different set of

Wannier functions and a different tunneling strength. Second, we see that the lowest band is simply a cosine—therefore we have solved for the band structure without even defining what the basis Wannier functions are! Third, the amplitude of the cosine function is given by the tunneling strength t . This gives us a good clue as to how to determine the appropriate tunneling given a lattice depth V_0 —simply find a t that matches the amplitude of the lowest band, which becomes sinusoidal in the deep lattice limit.

The precise form of the Wannier functions depends on both the depth of the lattice and the band being reproduced. It is not necessary for us to find their full expression, as the band structure can be calculated without them. The definition, however, is

$$|j\rangle = \int_{\text{BZ}} e^{i\phi(q) - iqja} |q\rangle dq, \quad (2.48)$$

where the integral is over the Brillouin zone, from $-k_L$ to k_L , a is the lattice spacing $\lambda_L/2$, and $|q\rangle$ is the Bloch wavefunction at crystal momentum q , and $\phi(q)$ is the phase associated with each Bloch wavefunction. The Bloch wavefunctions individually have arbitrary phase. The phase plays an important role in combining the Bloch wavefunctions into a Wannier function, finding the proper phase relationship to make the wavefunction maximally localized at each site [?].

2.5.3 Pulsing vs adiabatic loading of the lattice

The lattice depth parameter $V_0/4$, for a range of values, can be well calibrated experimentally by pulsing on the lattice. Here, the word pulsing indicates that the lattice is turned on fully non-adiabatically, if not instantaneously, such that the original bare momentum state is projected onto the lattice eigenvector basis, as shown in Figure 8a. If the atoms start out stationary in the trap, the bare state in

the momentum basis is simply

$$|\Psi_0\rangle = \begin{pmatrix} \vdots \\ 0 \\ 0 \\ 1 \\ 0 \\ 0 \\ \vdots \end{pmatrix}, \quad (2.49)$$

as depicted in Figure 8b.

Since the lattice eigenvector basis is distinct from the bare one, instantaneously turning on the lattice will necessarily excite the atoms into a superposition of lattice eigenstates, each evolving with a different phase according to the eigenenergy while the lattice is on, as shown in Figure 8c. Then, when the lattice is snapped back off, the wavefunction is projected back into the bare basis, and the varying phase accumulation results in a beating of the different momentum orders, see Figure 8d. This can be calculated simply by using the time evolution operator

$$|\Psi(t)\rangle = e^{-iH_L t/\hbar} |\Psi_0\rangle. \quad (2.50)$$

By pulsing on the lattice for variable amounts of time t , we can obtain fractional populations in the different momentum states. Time-of-flight imaging captures the momentum distribution of the cloud, and the different entries of $\Psi(t)$ in the momentum basis will thus appear as different clouds on the absorption image, as shown in Figure 7a. The fractional population in these clouds corresponds to a measurement of $|a_j|^2$. Typically for our values of the lattice depth $V_0 < 10E_L$, it is sufficient to simply count three central momentum orders, $k = q, q \pm 2k_L$. Then, we can fit eqn.

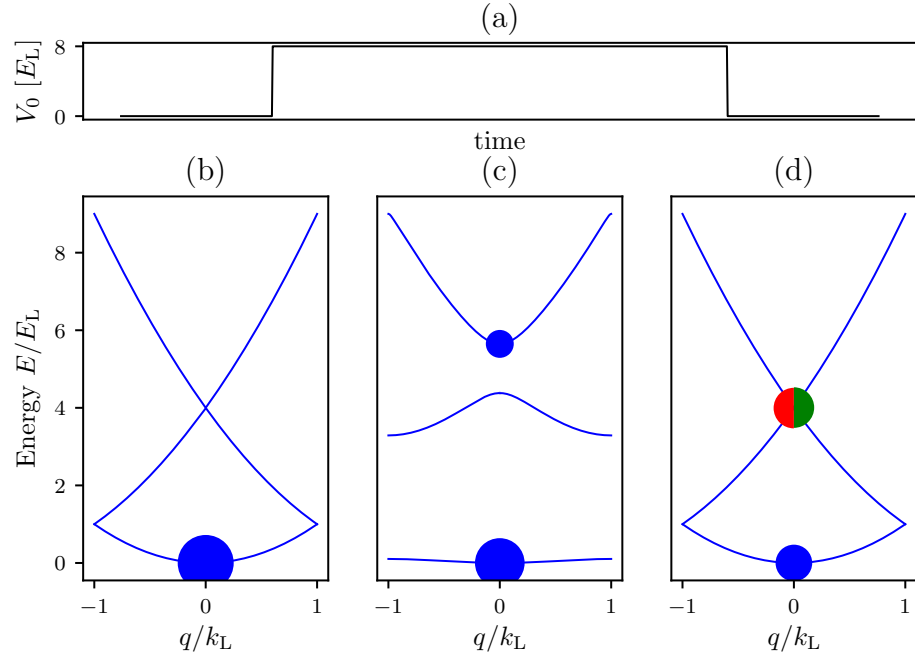


Figure 6: Lattice pulsing. (a) Lattice depth as a function of time during a pulsing experiment. The lattice is turned on instantaneously at $t = 0$ and held on for a variable amount of time until being turned off instantaneously at a final time $t = t_f$. (b) Atomic population before $t = 0$. The dispersion relation is that of a free particle, and all of the atoms start out at $q = 0$ in the lowest energy level. Here, the area of the dots is proportional to the fractional population in the energy state. (c) Atomic population after the lattice is turned on for a lattice depth of $V_0 = 8.0E_L$. The energy spectrum now shows the lattice band structure, and some atomic population is projected onto the excited bands. (d) Atomic population after the lattice is snapped off at $t_f = 150 \mu\text{s}$. The wavefunction is projected back onto the bare states, with some fraction (blue circle) in the lowest band at $k = 0$ and some fraction in the excited band, with equal population being projected onto the $k = 2k_L$ (green) and $k = -2k_L$ (red).

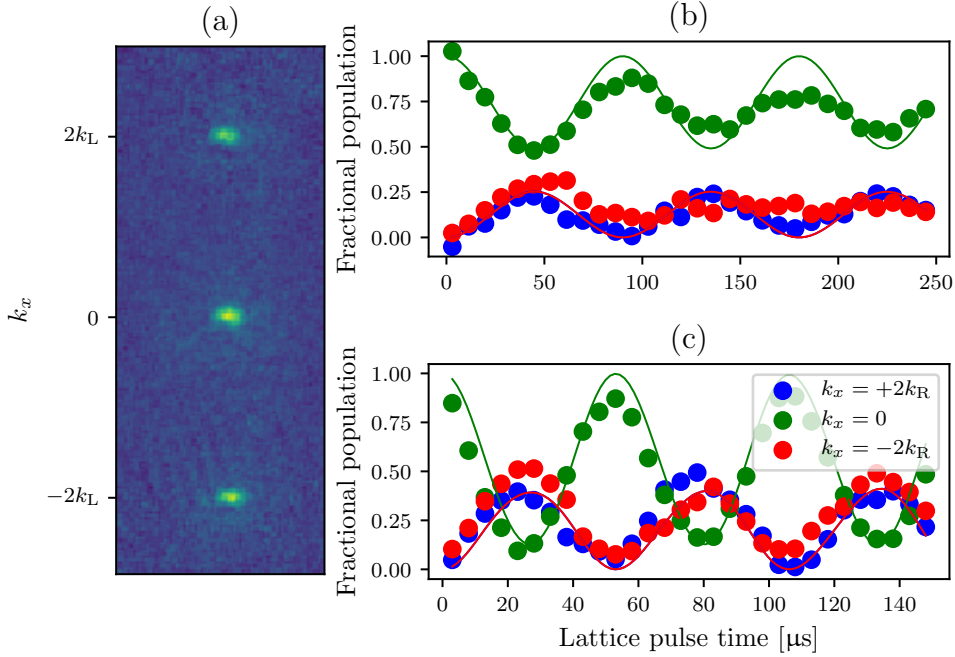


Figure 7: Lattice pulsing for calibration. (a) An example time-of-flight image from a pulsing experiment. The three different clouds are different momentum orders. (b) Fractional populations in the different momentum orders as a function of pulsing time at a low lattice power. Data is indicated by dots and best-fit theory is represented by lines. The lattice depth from fit is $V_0 = 5.57 \pm 0.07 E_L$. (c) Fractional populations in the different momentum orders as a function of pulsing time at a higher lattice power. Data is indicated by dots and best fit theory is represented by lines. The lattice depth from fit is $V_0 = 12.69 \pm 0.07 E_L$.

2.50 to the data with fitting parameter V_0 , thus deducing the lattice depth. Some examples of these pulsing experiments are presented in Figure 7b,c.

In contrast to pulsing, adiabatic loading turns the lattice on slowly, such that the atomic wavefunction starting in the bare ground state can continuously adjust to remain in the ground state of the current Hamiltonian, without projecting onto any of the higher bands. This process is illustrated in Figure 8. The adiabatic timescale depends on the spacing between the ground and next excited band (or if starting in a different eigenstate, the nearest eigenstate). If the energy difference between the ground and first excited state is ΔE , the timescale on which the lattice

is turned on must fulfill $t \gg h/\Delta E$.

2.6 Raman and rf coupling

In this section, we will introduce Raman and rf coupling between the hyperfine sublevels of the ground state of ^{87}Rb . While we will focus on the $F = 1$ and $F = 2$ manifolds of this ground state due to their relevance to the experiments described in Chapters ?? and ??, the discussion can be easily extended to any value of F .

2.6.1 Rf coupling Hamiltonian

For the $F = 1$ manifold, there are three available spin states $m_F = 0, \pm 1$. There are many ways of introducing coupling terms between the different hyperfine states. Here, we will explain two methods: rf coupling and Raman coupling. Rf coupling is a radio-frequency oscillating magnetic field, in our case produced by a pair of circular coils in series side by side above the atoms (see [19]). Assuming the rf oscillating field is polarized along the \mathbf{e}_x , with the bias field along \mathbf{e}_z , the coupling Hamiltonian is given by $H_{\text{rf}} = \mu_B g_F \hat{\vec{F}} \cdot \vec{B} = \mu_B g_F \hat{F}_x B_x \cos(\omega t)$, where $2\pi\omega$ is the rf frequency. The schematic of this setup is shown in Figure 9.

The eigenstates of the bare Hamiltonian H_0 are the constituent m_F states. The eigenstates of the coupled Hamiltonian $H_0 + H_{\text{rf}}(t)$ can be expressed as a linear superposition of the bare eigenstates $\Psi(\vec{x}, t) = \sum_{m_F} c_{m_F}(t) \phi_{m_F}(\vec{x}) e^{-i\omega_{m_F} t}$. The Hamiltonian in this basis can then be written as [?]

$$H_{\text{rf}} = H_{\text{KE}} + \hbar \begin{pmatrix} 0 & \Omega \cos(\omega t) e^{-i(\omega_z - \epsilon)t} & 0 \\ \Omega \cos(\omega t) e^{-i(\omega_z - \epsilon)t} & 0 & \Omega \cos(\omega t) e^{-i(\omega_z + \epsilon)t} \\ 0 & \Omega \cos(\omega t) e^{i(\omega_z + \epsilon)t} & 0 \end{pmatrix}, \quad (2.51)$$

where $\omega_z = (\omega_1 - \omega_{-1})/2$, ϵ is the quadratic Zeeman shift, and Ω is the Rabi fre-

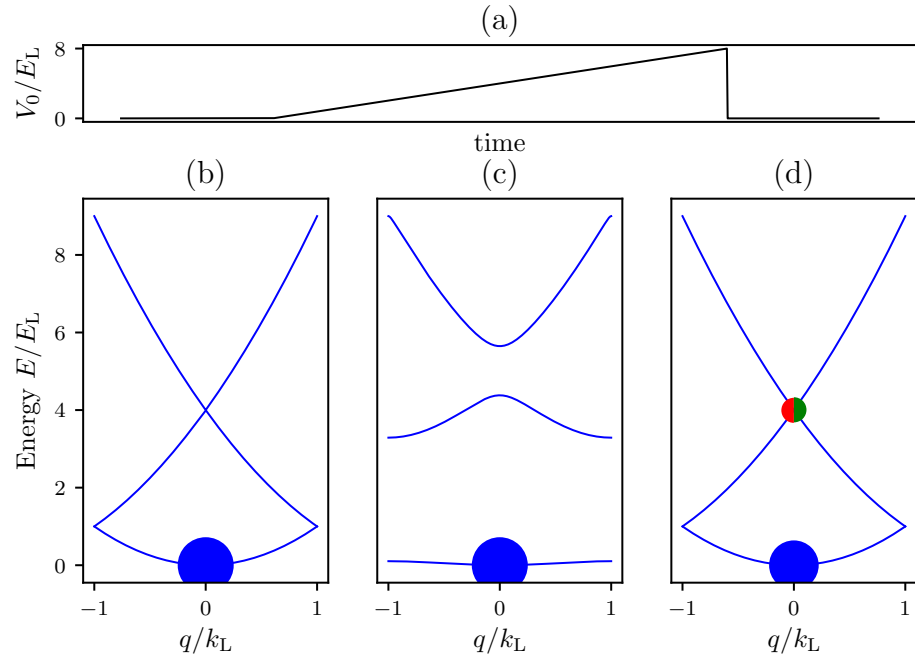


Figure 8: Adiabatic lattice loading. (a) Lattice depth as a function of time during adiabatic turn-on. The lattice is ramped on starting at $t = 0$, slowly increasing to a final lattice depth and turned off instantaneously at a final time $t = t_f$. (b) Atomic population before $t = 0$. All atoms are at $k = 0$ in the lowest bare band. (c) Atomic population after the lattice is turned on adiabatically to a lattice depth of $V_0 = 8.0E_L$. All atoms remain in the lowest band, but the band is no longer bare. (d) Atomic population after the lattice is snapped off. The wavefunction is projected back onto the bare states, with some fraction (blue circle) in the lowest band at $k = 0$ and some fraction in the excited band, with equal population being projected onto the $k = 2k_L$ (green) and $k = -2k_L$ (red). Since the lowest lattice band is a superposition of bare bands, some atoms are excited to the higher bare momentum states.

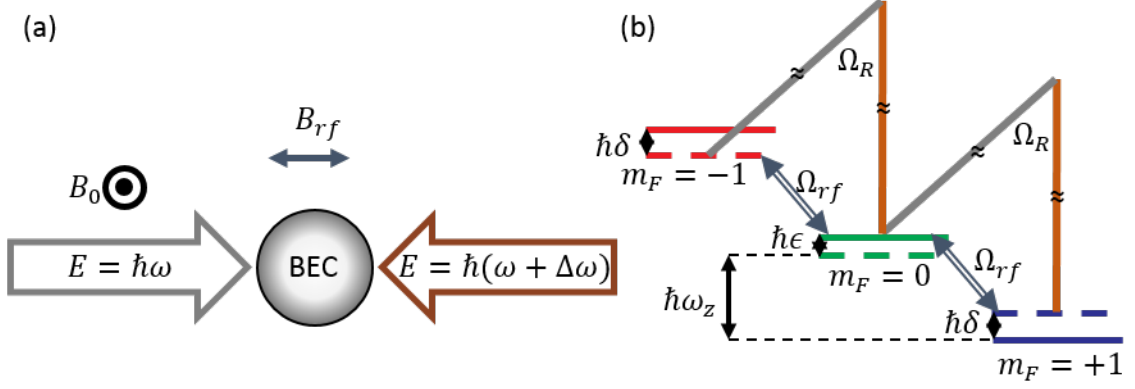


Figure 9: Raman and rf coupling schematic. (a) Beam geometry of the Raman beams and rf relative to the external field. The Raman beams have a frequency difference $\Delta\omega$, and are linearly polarized in perpendicular directions. (b) Level structure of both Raman and Rf coupling for hyperfine states of the $F = 1$ manifold. The hyperfine splitting separates the levels by an energy $\hbar\omega_z$. The quadratic Zeeman shift ϵ lowers the energy of the $m_F = 0$ state, and the detuning δ of either the Raman or the rf fields shifts the energies of the $m_F = \pm 1$ states. Raman transitions are two-photon, exciting up to a virtual state and coming back down to an adjacent hyperfine state, with an accompanying momentum transfer. Rf couples adjacent hyperfine states directly. Figure taken from ref. [?]

quency, proportional to B_x . We can then transfer into the rotating frame $c'_{m_F} = e^{-im_F\delta t+i(1-m_F^2)\epsilon t}c_{m_F}$, where $\delta = \omega_z - \omega$. Then we apply the rotating wave approximation, that the fast oscillating terms average to zero over time scales of interest $e^{2i\omega t} \approx 0$, and obtain

$$H_{\text{rf}} = H_{\text{KE}} + \hbar \begin{pmatrix} \delta & \Omega/2 & 0 \\ \Omega/2 & -\epsilon & \Omega/2 \\ 0 & \Omega/2 & -\delta \end{pmatrix}, \quad (2.52)$$

or for any value of F

$$H_{\text{rf}} = H_{\text{KE}} + \hbar\delta F_z + \hbar\epsilon F_z^2 + \Omega F_x/2, \quad (2.53)$$

which reduces to the above form for $F = 1$ with an overall energy shift of $\hbar\epsilon\mathcal{I}$.

The band structure of this Hamiltonian can be seen in Figure 10, where we have diagonalized eqn. 2.52 for a range of momenta k_x (we have isolated k_x for comparison with Raman coupling, as will be seen in the next section). The parabolas are simply the free particle dispersion relations along one dimension, with three bands arising from the three available spin states. It is convenient to define the magnetization of an eigenstate $m = \sum_{m_F} m_F p_{m_F}$, where p_{m_F} is the fractional population in the m_F state. We have indicated the magnetization of the eigenstate by coloring the eigenenergies, with $m = -1$ in red, $m = 0$ in green, and $m = +1$ in blue. In Figure 10a, both the detuning and the coupling strength are zero. Therefore, there are simply three free particle dispersion curves, each exactly correlated with a particular spin state, the $m_F = \pm 1$ are degenerate and the $m_F = 0$ state is slightly offset by the quadratic shift $\hbar\epsilon$. In Figure 10c, the coupling strength is again zero, but the detuning has been turned on, lifting the degeneracy between the $m_F = \pm 1$ states. Figure 10b,d shows the same conditions as a,c, respectively, but with the coupling strength turned on. In Figure 10b, where the detuning is zero and the quadratic shift is negligible compared to the coupling strength, all states average to a magnetization of zero—the $m_F = \pm 1$ states are symmetrically populated. In Figure 10d, this symmetry is broken by the presence of a detuning.

2.6.2 Raman coupling Hamiltonian

The counter-propagating Raman beams, as seen in Figure 9, couple the same states as the rf. They do so via the vector light shift created by the pair of beams. The electric field due to the right going beam (red in Figure 9a) is $\vec{E} = E_0 \exp(i k_R x - i\omega t) \mathbf{e}_y$, where E_0 is the amplitude of the electric field and $\hbar k_R = h/\lambda_R = \hbar\omega/c$. The electric field from the left going beam (gray in Figure 9b) is $\vec{E} = E_0 \exp(-i k_R x - i(\omega + \Delta\omega)t) \mathbf{e}_z$. This combines to give an effective field from the vector light shift [?] $B_{\text{eff}} \propto \vec{E} \times \vec{E}^* \propto -E_0^2 \cos(2k_R x + \Delta\omega t) \mathbf{e}_x$. Going through the same procedure as for

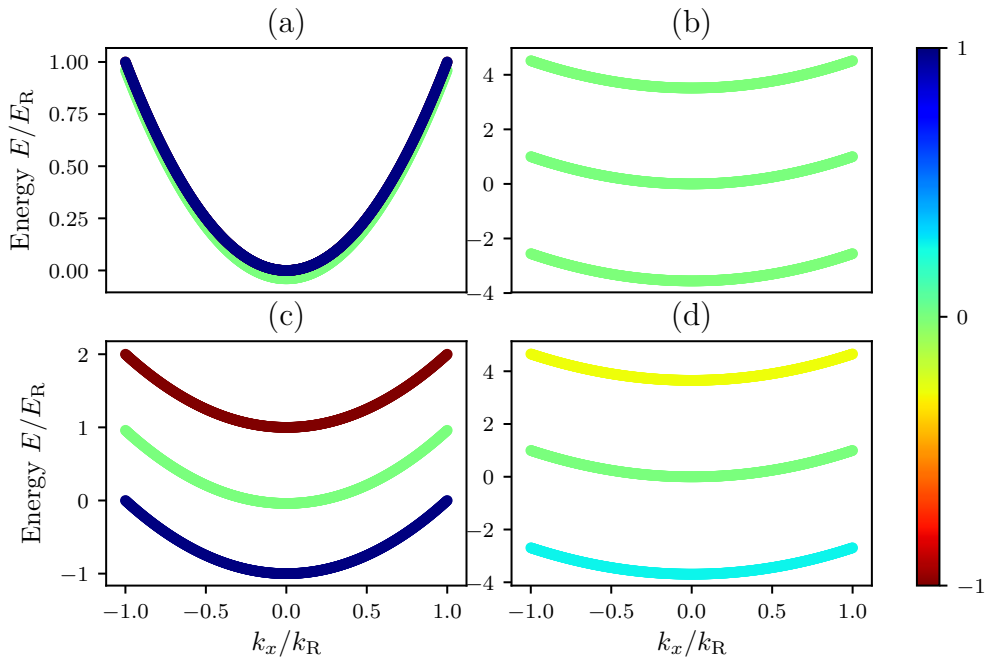


Figure 10: Band structure of the rf Hamiltonian, eqn. 2.52, in momentum space. For all plots, the quadratic Zeeman shift $\hbar\epsilon = 0.04E_R$, and the color represents magnetization, labeled by the colorbar. (a) $\hbar\Omega = 0$, $\hbar\delta = 0$. No coupling or detuning is present, so the only separation between the bands is due to the quadratic shift $\hbar\epsilon$. (b) $\hbar\Omega = 5.0E_R$, $\hbar\delta = 0$. (c) $\hbar\Omega = 0$, $\hbar\delta = 1.0E_R$. Even though the coupling strength is zero, the bands are separated by the detuning. (d) $\hbar\Omega = 5.0E_R$, $\hbar\delta = 1.0E_R$.

the rf coupling case, including the transfer into the rotating frame and the rotating wave approximation, we obtain the same Hamiltonian in the basis of bare spin states $| -1 \rangle, | 0 \rangle, | 1 \rangle$ but with an extra phase factor:

$$H_{\text{Raman}} = H_{\text{KE}} + \hbar \begin{pmatrix} \delta & \Omega/2e^{-i2k_{\text{R}}x} & 0 \\ \Omega/2e^{i2k_{\text{R}}x} & -\epsilon & \Omega/2e^{-i2k_{\text{R}}x} \\ 0 & \Omega/2e^{i2k_{\text{R}}x} & -\delta \end{pmatrix}, \quad (2.54)$$

where $\delta = \omega_z - \Delta\omega$.

This phase difference between the rf and Raman Hamiltonian has an intuitive physical explanation. In order to undergo a Raman transition, an atom first absorbs a photon from one beam, getting a momentum kick equal to the recoil momentum $\hbar k_{\text{R}}$. Then, to decay back down to an adjacent spin state, the atom undergoes stimulated emission into the field of the other (counter-propagating) beam, acquiring another recoil momentum kick in the same direction for a total of $2\hbar k_{\text{R}}\mathbf{e}_x$. Therefore, the Raman coupling Hamiltonian for $F = 1$, after transforming into the rotating frame and performing the rotating wave approximation, can be written in the same way as the rf Hamiltonian in eqn. 2.52 with the addition of a momentum kick—in real space, an acquired phase—of $e^{i2k_{\text{R}}x}$.

We can again make a basis transformation to get rid of this phase. Let us define $| -1' \rangle = \exp(-2ik_{\text{R}}x)| -1 \rangle = | k_x - 2k_{\text{R}}, -1 \rangle, | 0' \rangle = | 0 \rangle = | k_x, 0 \rangle, | 1' \rangle = \exp(2ik_{\text{R}}x)| 1 \rangle = | k_x + 2k_{\text{R}}, 1 \rangle$, where for third definition we went into the momentum basis and labeled the states by a combination of their momentum and spin state. Then, including the kinetic energy term along \mathbf{e}_x explicitly, we obtain the Hamiltonian in the new basis as:

$$H_{\text{Raman}} = H_{\text{KE}}^{(y,z)} + \begin{pmatrix} \frac{\hbar^2(k_x - 2k_{\text{R}})^2}{2m} + \hbar\delta & \hbar\Omega/2 & 0 \\ \hbar\Omega/2 & \frac{\hbar^2k_x^2}{2m} - \hbar\epsilon & \hbar\Omega/2 \\ 0 & \hbar\Omega/2 & \frac{\hbar^2(k_x + 2k_{\text{R}})^2}{2m} - \hbar\delta \end{pmatrix}. \quad (2.55)$$

It is convenient to define the Raman recoil energy as $E_R = \frac{\hbar^2 k_R^2}{2m}$. The band structure of this Hamiltonian is shown in Figure 11, for several representative parameter values, with the magnetization labeled by the color. Figure 11a shows the band structure in the limit of zero coupling and zero detuning, but where we have already gone into the basis $|k_x - 2k_R, -1\rangle, |k_x, 0\rangle, |k_x + 2k_R, 1\rangle$; therefore, the free particle parabola corresponding to the $m_F = 1$ spin states is shifted to center on $k_x = -2k_R$ and the $m_F = -1$ parabola is shifted to center on $k_x = 2k_R$. As the coupling is turned on to $\hbar\Omega = 1E_R$ in Figure 11b, the points where the parabolas cross become ‘avoided crossings’, separating into three bands where magnetization (and the underlying spin distribution) depends on the momentum k_x . As the coupling strength is turned up even further to $\hbar\Omega = 5E_R$ in Figure 11c, the lowest band goes from having three minima, one corresponding to each original spin state, to only one minimum. This transition happens at $\hbar\Omega = 4E_R$ [19]. In Figure 11d, we show the band structure again in the limit of zero coupling, but this time with a detuning of $\hbar\delta = 1.0E_R$. Note that the detuning tips the parabolas with respect to each other. Figure 11e shows the detuned system with coupling strength turned up to $\hbar\Omega = 1E_R$, still in the three minima regime but with avoided crossings creating three momentum and spin coupled bands. In Figure 11f, the detuned system is turned up to a coupling strength of $\hbar\Omega = 5E_R$, creating a single minimum, this time offset from $k_x = 0$.

We can write the general F version of the Raman coupled Hamiltonian in the basis $|k_x + m_F 2k_R, m_F\rangle$, where $-F \leq m_F \leq F$, as:

$$H_{\text{Raman}} = H_{\text{KE}}^{(y,z)} + \hbar^2(k_x \mathcal{I} + 2k_R F_z)^2 / 2m + \hbar\delta F_z + \hbar\epsilon F_z^2 + \Omega F_x / 2. \quad (2.56)$$

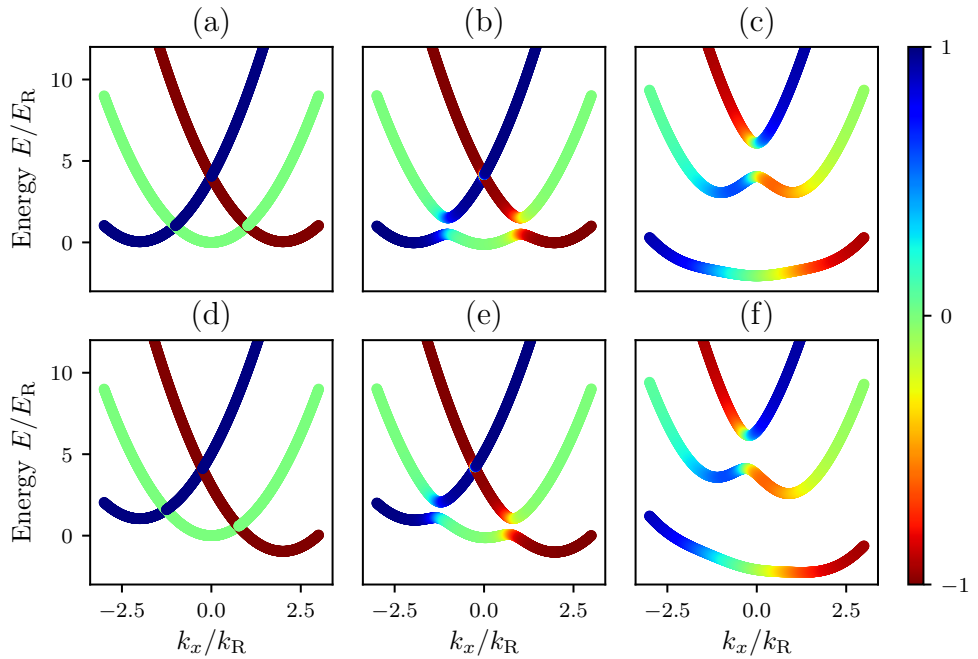


Figure 11: Band structure of the Raman Hamiltonian, eqn. 2.55, in momentum space. For all plots, the quadratic Zeeman shift $\hbar\epsilon = 0.04E_R$, and the color represents magnetization, labeled by the colorbar. (a) $\hbar\Omega = 0, \hbar\delta = 0$. (b) $\hbar\Omega = 1.0E_R, \hbar\delta = 0$. (c) $\hbar\Omega = 5.0E_R, \hbar\delta = 0.0$. (d) $\hbar\Omega = 0.0, \hbar\delta = 1.0E_R$. (e) $\hbar\Omega = 1.0E_R, \hbar\delta = 1.0E_R$. (f) $\hbar\Omega = 5.0E_R, \hbar\delta = 1.0E_R$.

2.6.3 Calibration of Raman and rf dressed states

To calibrate the rf and Raman coupling strengths, we take a similar approach to the 1-D lattice calibration: start in a pure spin state, for example $m_F = 0$, and turn the coupling on non-adiabatically to induce Rabi oscillations between the coupled states. Then, during time-of-flight, apply a Stern-Gerlach gradient pulse to separate the spin components and observe the fractional populations in different spin states as a function of Rabi oscillation time.

Figure 12a,b shows example images obtained in time-of-flight when pulsing on an rf coupling field for atoms in the $F = 1$ and $F = 2$ manifold, respectively. The Stern–Gerlach gradient pulse separates the spin components along the horizontal axis in the images. The fractional population in each state can then be obtained by summing up the optical depth in each cloud and dividing by the total optical depth. Similarly, Figure 13a shows an example time-of-flight image obtained when pulsing on a Raman coupling field on an $F = 1$ cloud initially in the $m_F = 0$ spin state. Here, the spin states are separated along the horizontal axis by the same Stern–Gerlach pulse. In addition, the recoil momentum obtained when undergoing a Raman transition separates the different spin states along the vertical axis—parallel to the Raman beams along \mathbf{e}_x . The direction of the Stern–Gerlach gradient was chosen purposefully to be perpendicular to the Raman direction \mathbf{e}_x for easy separation of the two effects.

These population oscillations can then be fit for coupling strength $\hbar\Omega$ and detuning $\hbar\delta$. Note that the quadratic Zeeman shift $\hbar\epsilon$ is set by the strength of the bias field B_0 and therefore often well known—it is not a fitting parameter. The theoretical predictions are obtained by applying the time evolution operator $U = \exp(-iH_{\text{Raman/rf}}t/\hbar)$ to an initial state Ψ in the appropriate basis. Figure 12c shows an example time series of rf pulsing in the $F = 1$ manifold, starting in the

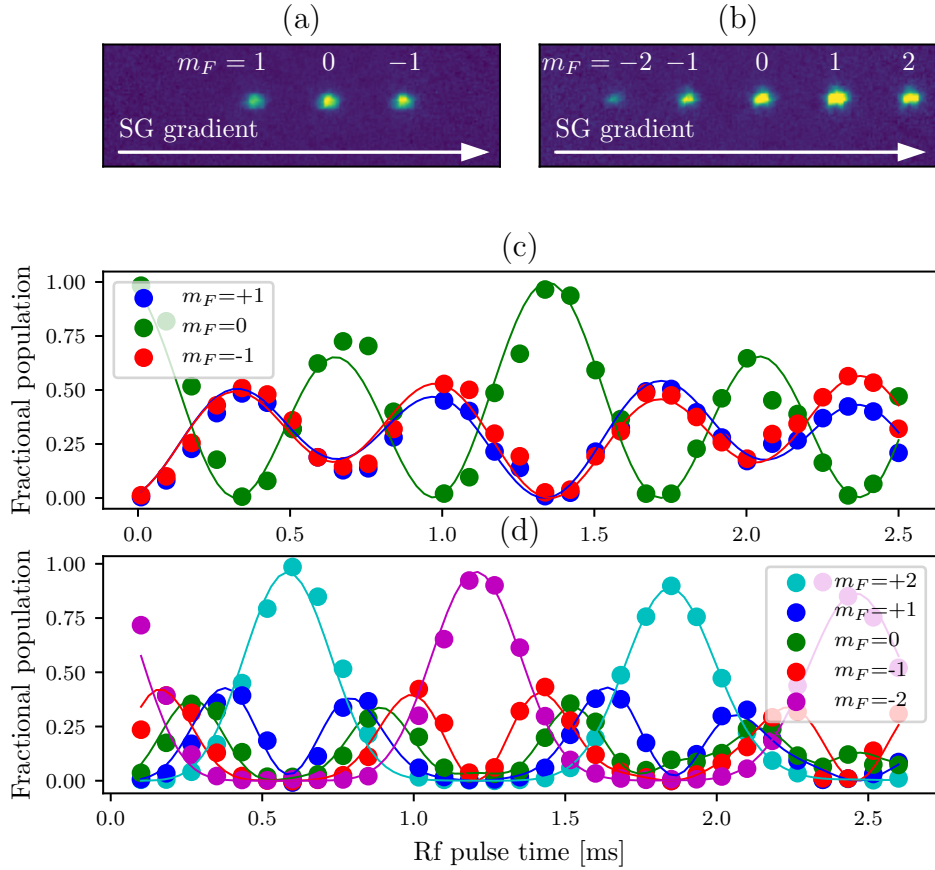


Figure 12: Pulsing on rf coupling. (a) Example time-of-flight image during an rf pulsing experiment in the $F = 1$ manifold. Spin states are separated via a Stern–Gerlach pulse along the horizontal direction. (b) Example time-of-flight image during an rf pulsing experiment in the $F = 2$ manifold. Here, 5 spin components are present. (c) Pulsing experiment in the $F = 1$ manifold. Dots represent fractional populations in different spin states measured from time-of-flight images, and lines represent best-fit theory curves. Fitted parameters are $\hbar\Omega = (0.863 \pm 0.004)E_R$, $\hbar\delta = (-0.198 \pm 0.007)E_R$. (d) Pulsing experiment in the $F = 2$ manifold. Dots represent fractional populations in different spin states measured from time-of-flight images, and lines represent best-fit theory curves. Fitted parameters are $\hbar\Omega = (1.000 \pm 0.002)E_R$, $\hbar\delta = (-0.061 \pm 0.001)E_R$. $\hbar\epsilon = 0.038E_R$ for all panels.

$m_F = 0$ state. The lines of best fit are overlayed on experimental data, extracting fit parameters $\hbar\Omega = (0.863 \pm 0.004)E_R$ and $\hbar\delta = (-0.198 \pm 0.007)E_R$. Figure 12d shows an example time series of rf pulsing in the $F = 2$ manifold, starting in the $m_F = -2$ state. Here, the extracted fit parameters were $\hbar\Omega = (1.000 \pm 0.002)E_R$ and $\hbar\delta = (-0.061 \pm 0.001)E_R$.

Figure 13b shows an example time series of Raman pulsing in the $F = 1$ manifold, starting in the $m_F = 0$ state, with fitted parameters $\hbar\Omega = (1.47 \pm 0.01)E_R$ and $\hbar\delta = (0.004 \pm 0.024)E_R$. Note that although the coupling strength is almost double the rf coupling strength in Figure 12c, the contrast (peak to peak oscillation of the fractional population in, say, the $m_F = 0$ state) is much lower in the Raman data than in the rf. This is a direct consequence of the recoil momentum transfer, and can be understood by looking at the band structure. For rf, the coupled bands at initial momentum $k_x = 0$ are separated by the coupling strength, see Figure ??b. For Raman, even at zero coupling strength, due to the shifting of the parabolas by $2k_R$, and $k_x = 0$ the higher bands are $\hbar^2(2k_R)^2/2m = 4E_R$ separated from the lower bands. Therefore, the energy difference is larger and the fraction in the excited band will be lower, leading to lower contrast.

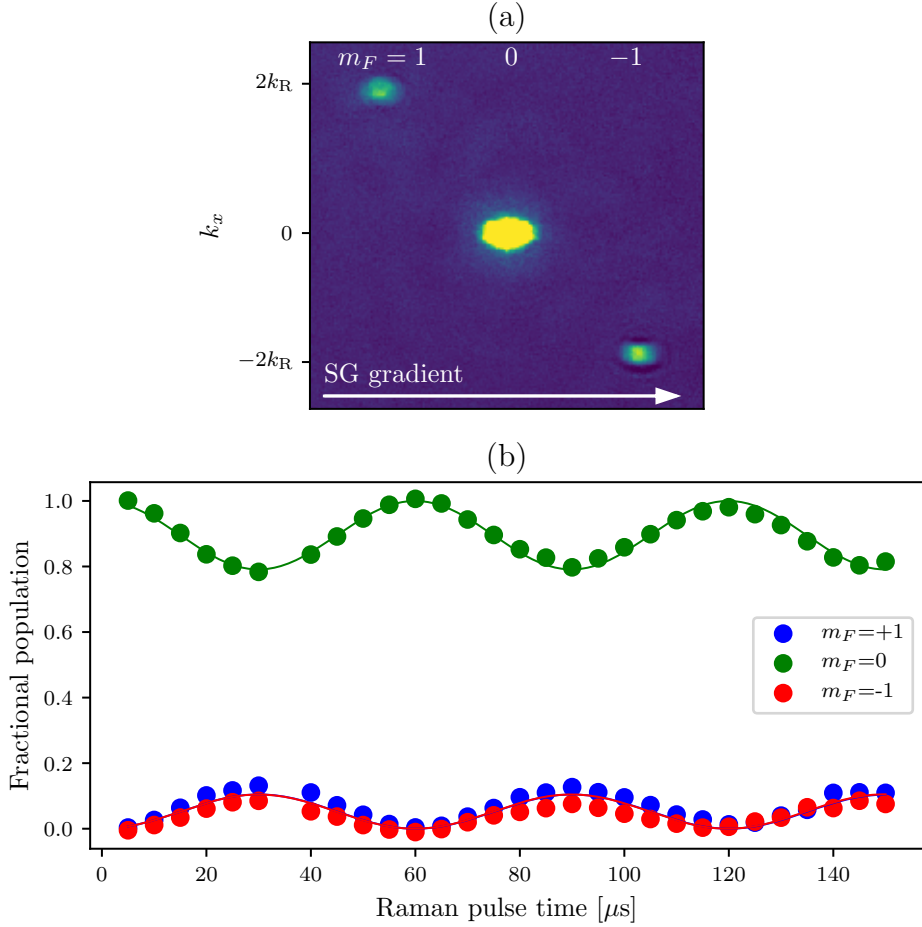


Figure 13: Pulsing on Raman coupling. (a) Example time-of-flight image during a Raman pulsing experiment in the $F = 1$ manifold. A Stern–Gerlach pulse during time-of-flight separates different spin components along the horizontal direction, and different momentum orders fly apart along the vertical direction. (b) Fractional population in different spin states during a Raman pulsing experiment as a function of time. Dots represent data and lines represent a best fit from theory. The fitted parameters are $\hbar\Omega = (1.47 \pm 0.01)E_R$, $\hbar\delta = (0.004 \pm 0.024)E_R$. The quadratic Zeeman shift was $\hbar\epsilon = 0.038E_R$.

Chapter 3: Ultracold Gases and the RbK apparatus

In this chapter we introduce the basics of ultracold quantum gases. When cooled to extremely low temperatures, bosonic atoms form Bose Einstein condensates, described in sec. ???. Fermionic atoms do not undergo a phase transition, but gradually become degenerate, forming what's known as a degenerate Fermi Gas, described in sec. ???. We then give a basic overview of the rubidium-potassium (RbK) apparatus at NIST, on which the work described in this thesis was done, in sec. ???. We detail some of the changes that have been made to the apparatus since it was last documented.

3.1 Bose-Einstein condensation

In this section, we give some basic background on Bose-Einstein condensation, relevant to ^{87}Rb atoms cooled in our apparatus.

3.1.1 Phase transition of a non-interacting Bose gas

Bose gases are characterized by the Bose-Einstein distribution giving the number of atoms $n(E_j)$ occupying each energy eigenstate E_j as

$$n(E_j) = \frac{1}{e^{(E_j - \mu)/k_B T} - 1}, \quad (3.1)$$

where k_B is the Boltzmann constant, T is the temperature in Kelvin, and μ is the chemical potential. Assuming the total atom number N is fixed, the chemical

potential $\mu(T, N)$ ensures that the total occupation $\sum_j n(E_j) = N$.

The Bose distribution leads to Bose-Einstein condensation, the collapse of a macroscopic fraction of the atoms into the ground state. This comes as a direct consequence of the Bose distribution's characteristic -1 in the denominator. Consider the occupation number $n(E_j)$. It must remain positive, as a negative occupation number is unphysical. This implies the quantity $e^{(E_j - \mu)/k_B T}$ must remain greater than 1, or $(E_j - \mu)/k_B T > 0$ for all E_j . Therefore, $\mu \leq E_0$, where E_0 is the ground state energy.

Then, for a given temperature T , there is a maximum occupation number for each excited state given by $n(E_j) = \frac{1}{e^{E_j/k_B T} - 1}$. The only energy state whose occupation number is unbounded is the ground state, as $n(E_0)$ tends toward infinity as μ tends towards 0. Therefore, as the temperature decreases, the maximum occupation of each excited state decreases until they can no longer support all N of the atoms. The remaining atoms then have no choice but to collapse into the lowest energy level and Bose condense.

We will show this quantitatively for the case of a 3-D harmonically trapped gas of non-interacting atoms, relevant to the experiments described in this thesis [1]. It is convenient to define the fugacity $\zeta = e^{\mu/k_B T}$, and re-write the Bose-Einstein distribution for some eigenstate E_j as

$$n(E_j) = \frac{\zeta}{e^{E_j/k_B T} - \zeta}. \quad (3.2)$$

The harmonic oscillator potential can be written as

$$V(r) = \frac{1}{2}m(\omega_x^2x^2 + \omega_y^2y^2 + \omega_z^2z^2), \quad (3.3)$$

where ω_x , ω_y and ω_z are the angular trapping frequencies along \mathbf{e}_x , \mathbf{e}_y , and \mathbf{e}_z . The

eigenenergies with this potential are

$$E(j_x, j_y, j_z) = \left(\frac{1}{2} + j_x\right)\hbar\omega_x + \left(\frac{1}{2} + j_y\right)\hbar\omega_y + \left(\frac{1}{2} + j_z\right)\hbar\omega_z. \quad (3.4)$$

In order to find μ , we must find $\sum_{j_x, j_y, j_z} n(E(j_x, j_y, j_z))$ and set it equal to N . This task is greatly simplified by going to the continuum limit and finding the density of states. To do this, we neglect the zero-point energy (setting $E_0 = 0$, the effects of the zero-point energy are discussed in [2] section 2.5) and assume there is on average one state per volume element $\hbar^3\omega_x\omega_y\omega_z$. Then, the total number of states with energy less than or equal to some value ϵ is given by the volume of a prism made between points $(j_x, j_y, j_z) = (0, 0, 0), (\epsilon, 0, 0), (0, \epsilon, 0)$ and $(0, 0, \epsilon)$ in units of the volume element:

$$G(\epsilon) = \frac{\epsilon^3}{6\hbar^3\omega_x\omega_y\omega_z}. \quad (3.5)$$

The density of states is given by

$$g(\epsilon) = \frac{d}{d\epsilon}G(\epsilon) = \frac{\epsilon^2}{3\hbar^3\omega_x\omega_y\omega_z}. \quad (3.6)$$

Note that the occupation of the ground state is not included in this continuum picture. We can therefore use it only to calculate the total number of atoms in all of the excited states:

$$N_{\text{ex}} = \int_0^\infty d\epsilon g(\epsilon)n(\epsilon) = \int_0^\infty d\epsilon \frac{\epsilon^2}{3\hbar\omega_x\omega_y\omega_z} \frac{\zeta}{e^{\epsilon/k_B T} - \zeta} = \frac{(k_B T)^3}{\hbar^3\omega_x\omega_y\omega_z} \text{Li}_3(\zeta), \quad (3.7)$$

where $\text{Li}_3(\zeta)$ is the polylogarithm function¹. We define the mean trapping frequency $\bar{\omega} = (\omega_x\omega_y\omega_z)^{1/3}$ and the harmonic oscillator energy as $\hbar\bar{\omega}$, with the thermal energy

¹This calculation was done with Wolfram Alpha, not Russian algebra skills

in harmonic oscillator units $\tau = k_B T / \hbar \bar{\omega}$, giving

$$N_{\text{ex}} = \tau^3 \text{Li}_3(\zeta). \quad (3.8)$$

Finding the occupation number of the ground state from the Bose-Einstein distribution

$$N_0 = \frac{\zeta}{1 - \zeta}, \quad (3.9)$$

we can then find the chemical potential, or equivalently the fugacity ζ , to satisfy

$$N = N_0 + N_{\text{ex}}. \quad (3.10)$$

This is a transcendental equation that can only be solved numerically. We present an example of the solution in Figure ???. Here, we have calculated the fractional population in different harmonic oscillator energy levels for three different temperatures, using trapping frequencies $\omega_x = \omega_y = \omega_z = 2\pi \times 50$ Hz, and atom number $N = 10^6$. For energies above the ground state (dots in the figure), we binned 50 energy levels together, such that each dot represents the total fractional population in 50 adjacent levels. This was obtained by integrating eqn. ?? from $\epsilon - 25\hbar\bar{\omega}$ to $\epsilon + 25\hbar\bar{\omega}$. The stars represent the fractional population in just the ground state, calculated from eqn. ???. Note that at temperature $T = 255$ nK (red), the ground state population is consistent with a continuous extrapolation from the excited state populations and is almost zero. At lower temperatures, $T = 180$ nK (blue) the ground state population is in excess of any reasonable extrapolation from the excited state fractions, and at $T = 80$ nK (green) almost all the atoms are in the ground state.

The onset of Bose-Einstein condensation occurs at a critical temperature T_c . This temperature is defined as the temperature at which the occupation number of excited states is equal to the atom number, i.e. when the atoms have occupied all

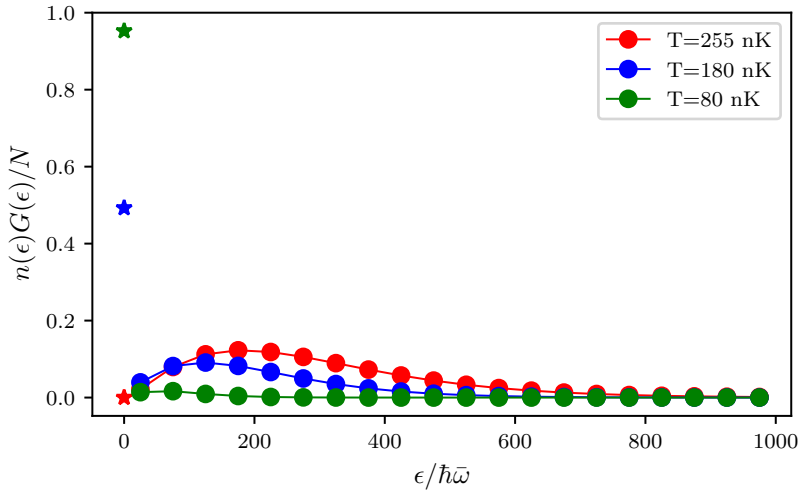


Figure 1: Occupation of energy states of a 3-D harmonic oscillator. The trapping frequencies are $\omega_x = \omega_y = \omega_z = 2\pi \times 50$ Hz, and the atom number is $N = 10^6$. Dots represent the total fractional population in 50 adjacent energy levels, including degeneracies. The stars represent the fractional population in just the ground state.

available excited states and any remaining atoms were forced to pile into the ground state. Since the maximal occupation of the excited states will occur at $\mu = 0$, the occupation of the excited state is bounded from above by $N_{\text{ex}}(\mu = 0)$, and the critical temperature is defined by

$$N = N_{\text{ex}}(\mu = 0, T = T_c) = \frac{(k_B T_c)^3}{\hbar^3 \omega_x \omega_y \omega_z} \text{Li}_3(\zeta = 1). \quad (3.11)$$

Using $\text{Li}_3(1) \approx 1.202$, we obtain for a given atom number and trapping frequencies

$$T_c = \frac{1.202 N}{k_B^3} \hbar^3 \omega_x \omega_y \omega_z. \quad (3.12)$$

For the parameters in Figure ??, $T_c = 225$ nK.

For temperatures below the critical temperature, the condensation fraction f_c —the fraction of atoms in the ground state—is directly related to the ratio of the

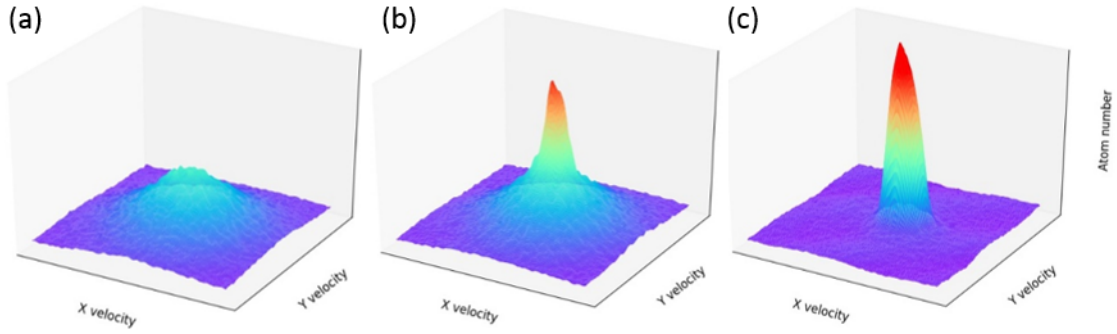


Figure 2: Time-of-flight images of atoms. (a) Above the critical temperature - the atoms are thermally distributed. (b) Below the critical temperature - about half of the atoms are condensed in the central peak. (c) Far below the critical temperature - almost all atoms are condensed in the central peak.

temperature to the critical temperature:

$$f_c = 1 - \frac{N}{N_{\text{ex}}} = 1 - \frac{(k_B T)^3}{\hbar^3 \omega_x \omega_y \omega_z} \text{Li}_3(\zeta = 1) = 1 - \left(\frac{T}{T_c} \right)^3, \quad (3.13)$$

where in the last step we have plugged in the definition of the critical temperature eqn. ??.

Figure ?? shows the progression towards condensation as the temperature of a cloud of ^{87}Rb is decreased below T_c . The images are obtained via a time-of-flight measurement (see section 2.4.1), where the atoms are allowed to expand freely, mapping the initial momentum to final position, imaged via absorption imaging (see section 2.4). The x and y axes represent momentum along x and y , while the z axis represents the number of atoms per spatial bin. The z axis momentum is integrated over. Figure ??a shows a cloud above the condensation temperature - the momentum distribution is nearly gaussian, given by the Maxwell-Boltzmann distribution. In fig. ??b, the temperature has been decreased below T_c , and about half the atoms have collapsed into the ground state, producing a large peak in atom number around zero momentum. In fig. ??c, the temperature has been decreased

even further and almost all the atoms populate the central peak - the distribution is no longer gaussian but a sharp peak around zero momentum.

3.1.2 Interacting Bose gas

In the previous section, we assumed there were no interaction between the atoms other than those enforced by statistics. In this section, we will relax this assumption somewhat and describe the condensed atomic state through its characteristic Gross-Pitaevskii equation.

Since condensation occurs at very low temperatures, and thus very low kinetic energies, we can assume that any scattering processes between the atoms are *s*-wave and can be described simply by a scattering length a (equivalent to assuming that the characteristic size of the atomic wavefunction, given by the thermal deBroigle wavelength, is large compared to the scale of the interatomic potential). For ^{87}Rb , relevant to experiments described in this thesis, the scattering length between two atoms in the $F = 2$ hyperfine state is $a = 95.44(7)a_0$ [3], where $a_0 = 5.29 \times 10^{-11}$ m is the Bohr radius. The short-range interaction between two particles can be approximated as a contact interaction with an effective strength U_0 as (see [2] section 5.2.1):

$$U(r_1, r_2) = U_0\delta(r_1 - r_2) = \frac{4\pi\hbar^2 a}{m}\delta(r_1 - r_2), \quad (3.14)$$

where m is the atomic mass and δ is the Dirac delta function. The full Hamiltonian of the many-body system is then

$$H = \sum_i \frac{p_i^2}{2m} + V(r_i) + U_0 \sum_{i < j} \delta(r_i - r_j), \quad (3.15)$$

where i labels the particles, p_i is the momentum, r_i is the position, and V is the external potential.

We make the mean field approximation by assuming that no interactions be-

tween two atoms take them out of the ground state, and hence all atoms can be assumed to be in the same single particle wavefunction, making the overall wavefunction

$$\Psi(r_1, r_2, \dots, r_N) = \prod_i^N \phi(r_i), \quad (3.16)$$

where ϕ is the single particle wavefunction. It is convenient to define the wavefunction of the condensed state, $\psi(r) = \sqrt{N}\phi(r)$, making the normalization $N = \int dr |\psi(r)|^2$.

The energy of this wavefunction under the Hamiltonian above is given by

$$E = \int dr \left[\frac{\hbar^2}{2m} |\nabla \psi(r)|^2 + V(r) |\psi(r)|^2 + \frac{1}{2} U_0 |\psi(r)|^4 \right]. \quad (3.17)$$

Given N particles, there are $N(N - 1)/2$ unique pairs of particles that can have a pairwise interactions, approximately equal to $N^2/2$ for large N . The N^2 is absorbed into the definition of ψ , but the factor of $1/2$ remains on the final interaction term. The task of finding the condensate eigenstate reduces to minimizing this energy under the normalization constraint $N = \int dr |\psi(r)|^2$. This can be done by using the method of Lagrange multipliers to minimize $E - \mu N$. Then, we can minimize this quantity by finding the point where the derivative with respect to ψ and ψ^* is zero. Taking the derivative with respect to ψ^* we obtain

$$-\frac{\hbar^2}{2m} \nabla^2 \psi(r) + V(r) \psi(r) + U_0 |\psi(r)|^2 \psi(r) = \mu \psi(r), \quad (3.18)$$

which is the Gross-Pitaevskii equation. This is a non-linear equation that generally needs to be solved numerically.

There is another approximation that can be made in cases where the atomic density is high enough that the interaction energy is significantly larger than the kinetic energy. Then, the kinetic term in the Hamiltonian can be neglected. This is

called the Thomas-Fermi approximation. In this approximation, the wavefunction is given simply by

$$|\psi(r)|^2 = \frac{\mu - V(r)}{U_0}. \quad (3.19)$$

Here, the probability density simply takes the shape of the inverted potential in which the atoms are held. In the case of a harmonically trapped BEC, it is shaped like an inverted parabola. The Thomas-Fermi radius, i.e. the extent of the particle wavefunction, is the point where the probability density goes to zero: $\mu - V(r_0) = 0$. For a harmonic trap, along any direction, this is given by $r_0^2 = 2\mu/m\omega^2$.

Figure ??a shows an absorption image of a small fraction of atoms in a BEC *in situ* (see section 2.4.1), meaning as it is in the trap - without expanding in time-of-flight. The x and y axes represent position, while color represents the atom number. Figure ??b shows the atom number integrated over the y -axis in blue. The red dashed lines represent the best fit line to a Thomas-Fermi distribution, here an inverted parabola. The black dashed lines represent the best fit of a Gaussian to the atomic distribution. The Thomas-Fermi distribution matches the atomic distribution more closely in the center where the density is high, but the Gaussian distribution does a better job at the tails of the distribution. This is due to the presence of some fraction of uncondensed atoms, which are well approximated by a Maxwell-Boltzmann distribution.

3.2 Degenerate Fermi Gas

In this section, we give some basic background on degenerate Fermi gases, relevant to ^{40}K atoms cooled in our apparatus.

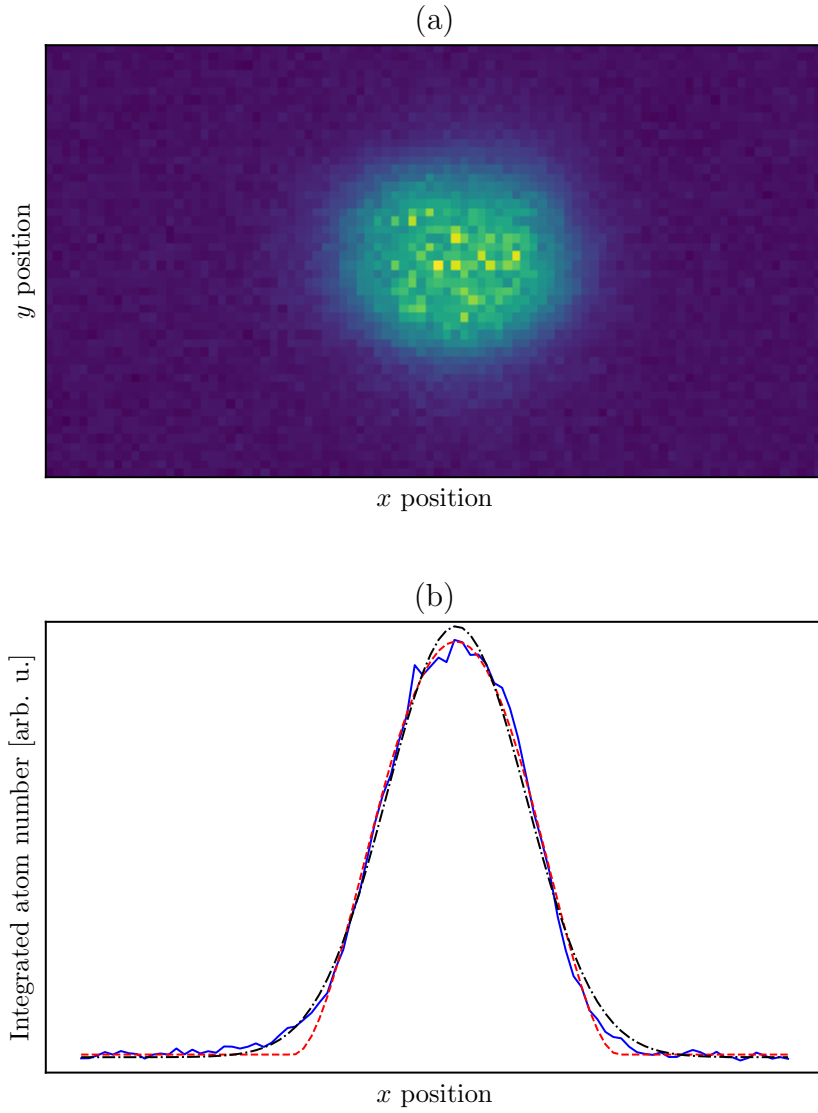


Figure 3: In situ measurement of Bose condensed atoms. (a) Absorption image taken of $\approx 1\%$ of the cloud. The x and y axes represent x and y position, while color represents the atom number. (b) The blue line represents atom number as a function of position along the x axis, integrated over the y axis. The black dashed line represents the best fit of a Gaussian function to the atomic distribution. The dashed red line represents the best fit of a Thomas-Fermi profile (integrated over the other two dimensions) to the atomic distribution.

3.2.1 Fermi statistics and the onset of degeneracy

The occupation of different energy levels E_j by Fermions is given by the Fermi-Dirac distribution:

$$n(E_j) = \frac{1}{e^{(E_j - \mu)/k_B T} + 1}. \quad (3.20)$$

The difference from the Bose-Einstein distribution is simply the sign of the 1 in the denominator. This has important implications, however. First, since e^x varies between 0 and ∞ , the occupation $n(E_j)$ varies between 1 and 0 - a consequence of the Pauli exclusion principle. Second, as the temperature T tends towards 0, there become two distinct cases: $E_j - \mu > 0$ and $E_j - \mu < 0$. If $E_j - \mu > 0$, $e^{(E_j - \mu)/k_B T}$ tends towards ∞ , and $n(E_j)$ tends towards 0. If $E_j - \mu < 0$, $e^{(E_j - \mu)/k_B T}$ tends towards 0, and $n(E_j)$ tends towards 1. Therefore, at $T = 0$, the energy states below the chemical potential μ are maximally occupied (with probability 1) and the energy states above the chemical potential are unoccupied.

We can use this to determine the chemical potential at $T = 0$ by constraining the total atom number:

$$N = \sum_j n(E_j) = \sum_{E_j < \mu} 1. \quad (3.21)$$

Again, we take the common example of the 3-D harmonic trap. Then the task reduces to simply finding the number of energy levels at or below a certain energy μ . This is given by eqn. ???. From this, we find the chemical potential at zero energy, which is known as the Fermi energy E_F , as

$$E_F = (6N)^{1/3} \hbar \bar{\omega}, \quad (3.22)$$

where $\bar{\omega} = (\omega_x \omega_y \omega_z)^{1/3}$ is the geometric mean of the three trapping frequencies.

From the Fermi energy, we can define the associated Fermi temperature T_F as

$$T_F = \frac{(6N)^{1/3} \hbar \bar{\omega}}{k_B}, \quad (3.23)$$

and the Fermi momentum $\hbar k_F$ as

$$\hbar k_F = \sqrt{2mE_F}, \quad (3.24)$$

where m is the mass of the Fermion.

For higher temperatures, we can solve for the chemical potential, or the fugacity ζ , by integrating the Fermi-Dirac distribution weighted by the density of states (eqn. ??) to obtain

$$N = \int_0^\infty \frac{\epsilon^2}{2\hbar^3 \bar{\omega}^3} \frac{\zeta}{e^{\epsilon/k_B T} + \zeta} = -\frac{(k_B T)^3}{\hbar^3 \bar{\omega}^3} \text{Li}_3(-\zeta), \quad (3.25)$$

where Li_3 is again the polylogarithm function. Again, this is a transcendental equation that can be solved numerically. However, in contrast to the BEC case, we do not have to consider the ground state occupation separately, as it is bounded by 1 like every other state.

We show an example of the occupation distribution for different temperatures in Figure ???. Here, we have used the same parameter values as for the BEC case: $N = 10^6$ and $\omega_x = \omega_y = \omega_z = 2\pi \times 50$ Hz. The Fermi temperature for these parameters is $T_F = 436$ nK. For illustrative purposes, we plot $n(\epsilon)$, unweighted by the density of states $g(\epsilon)$. At zero temperature (red line in the figure), only states below the Fermi energy are occupied. At higher temperatures, the distribution is smoothed out (green and orange lines) until at the Fermi temperature there is almost no significance to the Fermi energy.

In contrast with Bose-Einstein condensation, the transition to a Degenerate

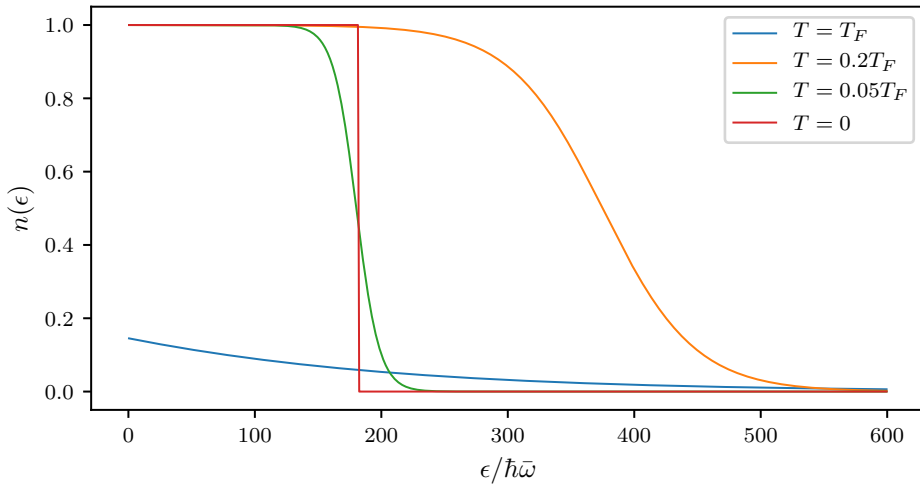


Figure 4: Occupation number as a function of energy for a Fermi gas of $N = 10^6$ atoms in a 3-D harmonic oscillator with frequencies $\omega_x = \omega_y = \omega_z = 2\pi \times 50$ Hz. The Fermi temperature for these parameters is $T_F = 436$ nK.

Fermi Gas (DFG) is not a phase transition, and there is no absolute measure of the onset of degeneracy. Instead, a Fermi gas can be considered degenerate when the occupation function $n(\epsilon)$ differs significantly from that of a thermal gas. This occurs when the temperature is of order $0.2T_F$.

3.2.2 Interactions and Feshbach resonances

Although the magnitude of the contact interaction U_0 for DFGs is not intrinsically different from that of BECs, there are two key differences. First, the Pauli exclusion principle forbids s -wave interactions between atoms of the same spin. Higher partial wave interactions are 'frozen out' at low temperatures, when the impact parameter of the collision becomes larger than the effective cross section of interactions (see [4], sec. 2.1.2). Therefore, in order to observe interactions, and indeed to cool the gas to degeneracy, another species needs to be present so that intraspecies s -wave interactions can occur. This can be a different atomic species or a different spin state of the same atom.

Second, the densities of standard DFGs ($\approx 10^{12}$ atoms/cm 3) are much lower than that of BECs ($\approx 10^{14}$ atoms/cm 3). Since the likelihood of two-body collisions is proportional to the atomic density ρ^2 , this leads to a much smaller effect of interactions in DFGs.

A widely used technique for enhancing interaction effects in DFGs (and to a more limited extent, BECs) is Feshbach resonances [5–9]. A Feshbach resonance occurs between two species (either atomic species or spin species of the same atom) when the open channel, i.e. the two particles independently in their external potential, energetically approaches a closed channel, i.e. a bound molecular state of the two species, shown schematically in Figure ??a.

Generally, the atoms in an open channel are energetically sensitive to a background magnetic field \vec{B} via the hyperfine interaction $H_B = -\vec{\mu} \cdot \vec{B}$, where μ is the magnetic dipole moment. Tuning the magnetic field should therefore tune the energy of the open channel with respect to the closed channel. The molecular bound state may also have an overall magnetic moment, but it is generally not identical to that of the two atoms in the open channel, and therefore varies differently with the background field. Figure ??b shows an example where the bound state has zero magnetic moment. Here, the energy of both the closed and open channel as a function of background magnetic field \vec{B} is plotted in the vicinity of a Feshbach resonance. The resonance occurs at a field magnitude B_0 where the energies of the two channels coincide.

Assuming there is at least infinitesimal coupling between the closed and open channels, as the energies of the two channels approach each other the perturbative correction term to the energy grows and the interaction between the atoms is affected. This is most easily seen in the *s*-wave case through changes in the scattering length a . In the case where there are no inelastic two-body channels, such as for the ${}^{40}\text{K}$ resonance discussed in this thesis, the interatomic scattering length as a

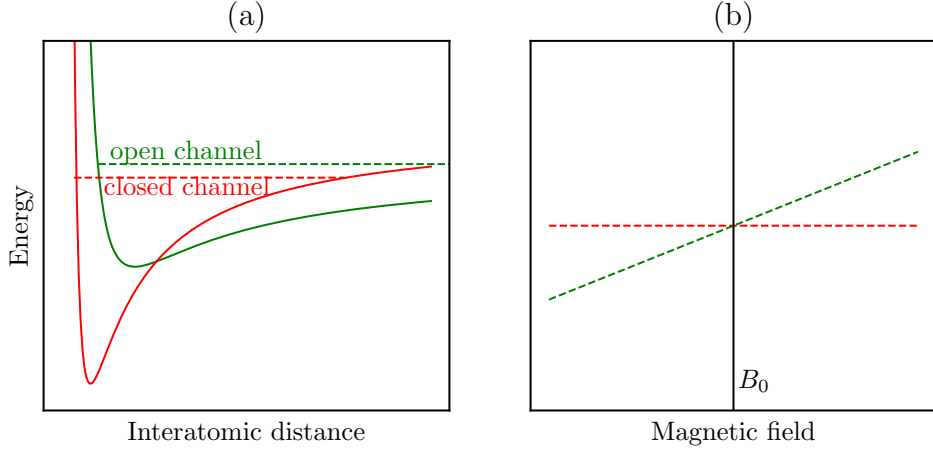


Figure 5: Schematic of a Feshbach resonance. (a) Pictoral representation of energy as a function of interatomic distance for an open channel (red) and closed channel (blue). (b) Energy as a function of background magnetic field B for the closed (blue) and open (red) channels. The energies coincide at the Feshbach resonance point B_0 .

function of background field is given by [10]

$$a(B) = a_{\text{bg}} \left(1 - \frac{\Delta}{B - B_0} \right), \quad (3.26)$$

where a_{bg} is the background scattering length, Δ is the width of the resonance, and B_0 is the field value at which the resonance occurs. The scattering length diverges at the resonance.

The tunability of interactions provided by Feshbach resonances has allowed for creation of molecular Bose-Einstein condensates from Fermi gases [11–13] as well as observation of the phase transition from the Bardeen-Cooper-Schrieffer (BCS) superconducting regime to the BEC regime at sufficiently low temperatures [14–17].

3.3 RbK apparatus

The rubidium-potassium (RbK) apparatus at NIST Gaithersburg has been previously detailed in [18–20]. In this thesis, we will give a brief overview of the apparatus and how it is used to produce BECs of ^{87}Rb and DFGs of ^{40}K , and only give

detailed documentation for those parts of the apparatus that differ from previous works.

A photograph of the main experiment is shown in Figure ???. This is mounted on an optical table, with the science chamber elevated above the surface of the table. The atoms start at the ovens (off to the right, not in the photograph) and travel down the Zeeman slower until they are trapped in the science chamber. The optical dipole trap laser, as well as the 1-D optical lattice laser, are located on the optical table and coupled into optical fibers, which are output on the main floor of breadboard before being sent towards the atoms. All other lasers are located on other optical table and brought over to the experiment table via optical fibers.

3.3.1 Laser beams

Figure ?? details the beam paths of the light going through the atoms. Figure ??a shows a side view of the apparatus. The up and down going MOT cooling beams are shown in red, reaching the atoms when the flipper mirrors M_{top} and M_{bottom} are flipped in. The down going probe beam, used for imaging along the $x - y$ axis both in situ and in time-of-flight, is shown in solid blue. The probe beam is split via a polarizing beam splitter cube to allow for both in situ and time-of-flight imaging of the same cloud, shown in the inset in fig. ??b and described in greater detail in sec. ???. The dashed blue line represents the upward going probe beam introduced for alignment purposes, described in greater detail in sec. ???. The kinematic base mirror (green in the figure) is removable, and only inserted when the alignment beam is in use.

Figure ??b show's a bird's eye view of the apparatus, with optics on the main floor breadboard. The slower cooling (solid dark blue) and slower repump (dashed dark blue) are coming in from the left to slow the atoms as they are moving through the Zeeman slower. The remaining four MOT cooling beams, coming from four

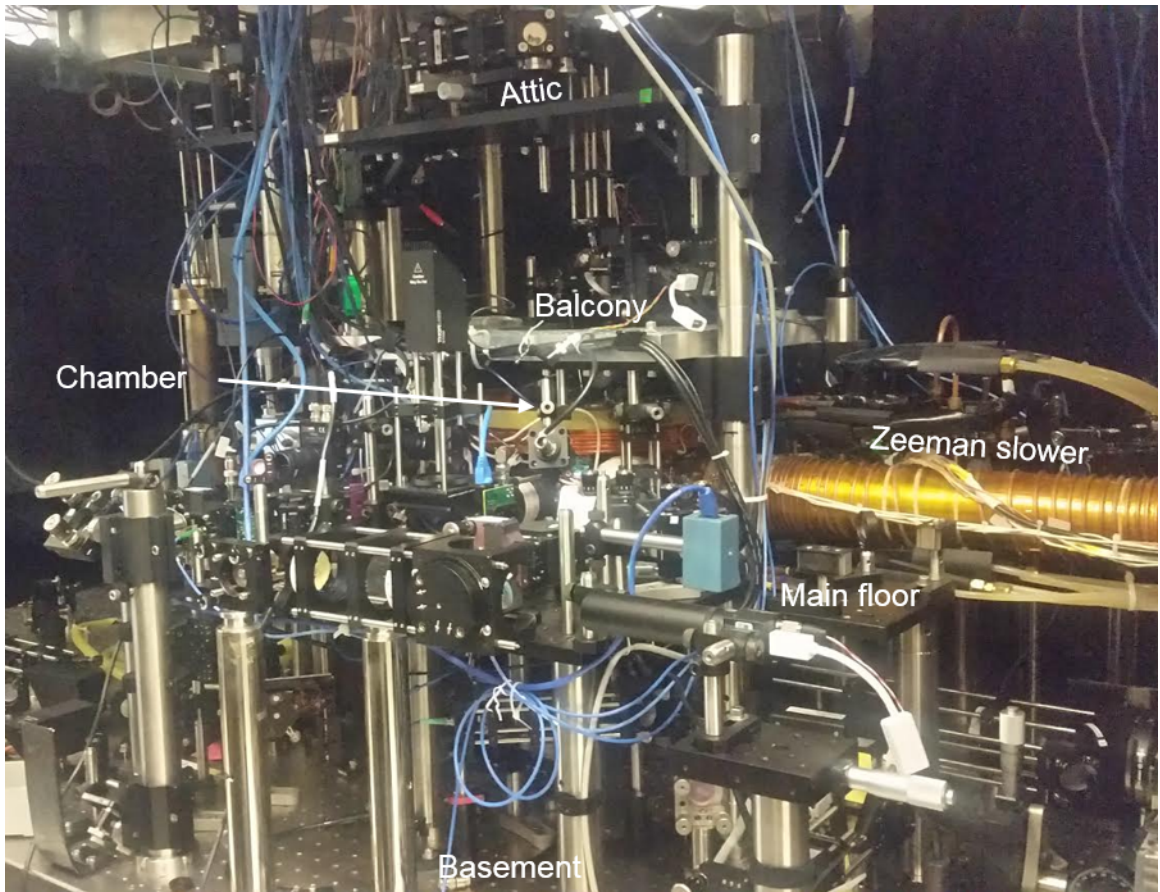


Figure 6: Photograph of RbK apparatus at NIST Gaithersburg. The main science chamber is at the center, hidden behind optics and coils. The Zeeman slower connects the atomic ovens (not shown) to the chamber. There are several levels of breadboards on which optics are mounted, labelled here as basement (surface of optical table), main floor, balcony and attic.

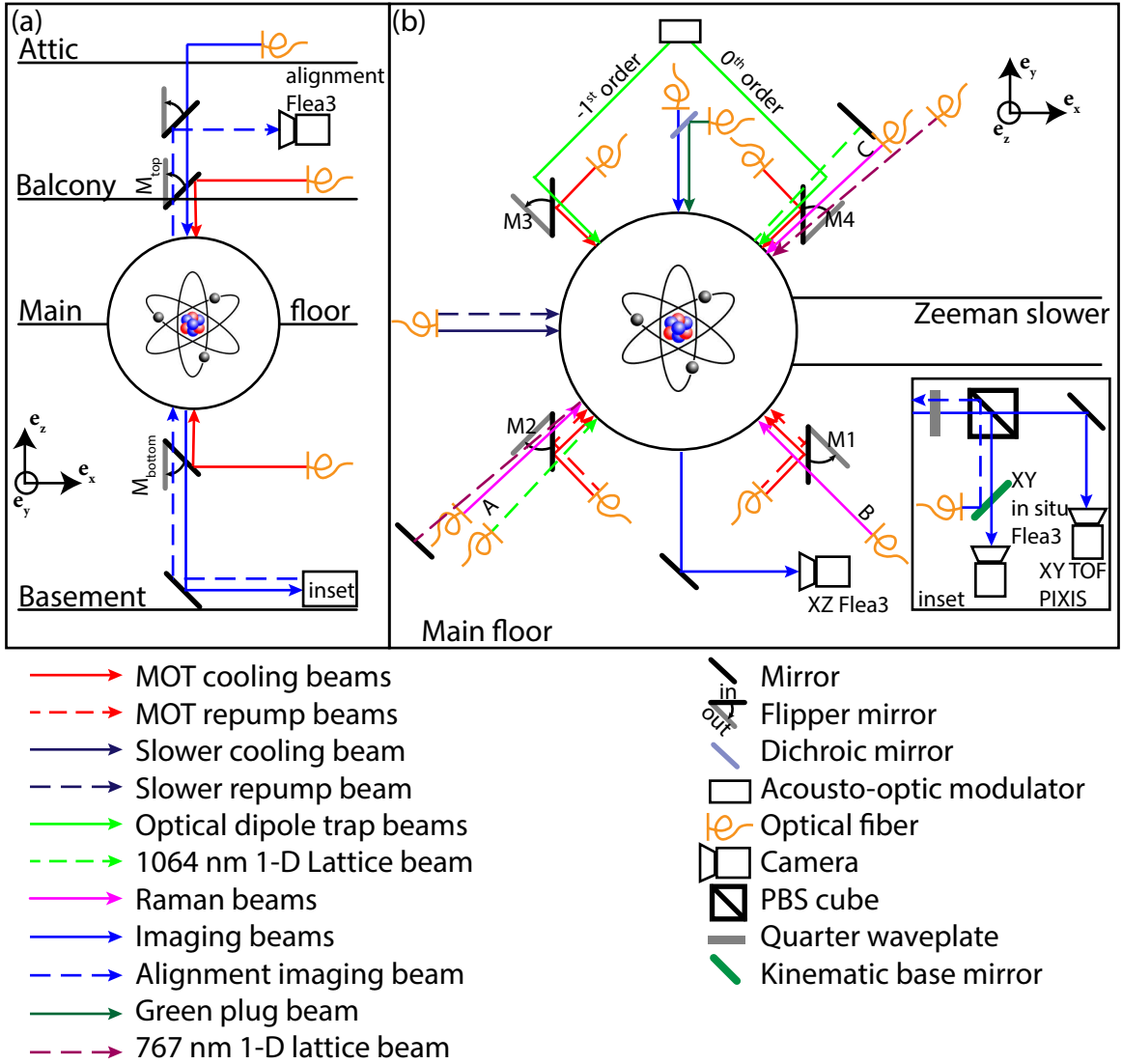


Figure 7: Schematic of RbK apparatus. (a) Side view of apparatus. Only beams propagating along the e_z direction through the atoms are pictured. (b) Top view of apparatus. Only beams propagating along the $x-y$ plane are shown. Schematic is not to scale and the angles are approximate.

opposing directions, are shown in red. They reach the atoms when their flipper mirrors, $M1 - 4$, are flipped in. All six flipper mirrors are computer controlled by the same digital channel, so they can be flipped in and out together. Only the beams going in through mirrors $M1$ and $M2$ are accompanied by MOT repump light, dashed red lines. The repump light for ^{87}Rb (both MOT and slower) comes from a Toptica DL-100 laser. The cooling light (MOT, slower) as well as imaging beams, come from a Toptica TA-100 tapered amplifier system. Both lasers are frequency referenced to a master laser, a toptica DL-pro, which is frequency stabilized to a ^{87}Rb atomic transition via saturated absorption spectroscopy (see section ??).

The optical dipole trap beams (solid green) come from the same 1064 nm laser (IPG YDL-30-LP), and are split via an acousto-optic modulator into two orders, which enter from opposite directions and intersect each other at approximately a 90 degree angle, providing confinement along all three axes. There is a 1-D optical lattice beam (dashed green), also 1064 nm (IPG YAR-10K-1064-LP-SF, seeded by a pick off from an NP Photonics seed laser), sent in past the $M2$ mirror and retro-reflected on the opposite end of the chamber to form a standing wave pattern. This was also used for experiments in Chapters ?? and ?. There is also another imaging beam, imaging the atoms along the x - z plane, going to a Flea3 camera.

There are three Raman beams (solid magenta): Raman A, entering past the flipped-out $M2$ mirror, Raman B, at 90 degrees to Raman A entering past the $M1$ mirror, and Raman C, counter-propagating with Raman A and entering past the $M4$ mirror. The Raman beams are derived from a tunable Coherent MBR-110 Ti:Sapphire laser seeded by a Coherent Verdi V-10 laser. For experiments described in Chapters ?? and ??, we used the Raman A and C beams.

When ^{40}K atoms are in use, the slower cooling, slower repump, MOT cooling, MOT repump and imaging beams are all a combination of frequencies for both ^{87}Rb and ^{40}K , fiber coupled before they were sent to the main experiment table. Both the

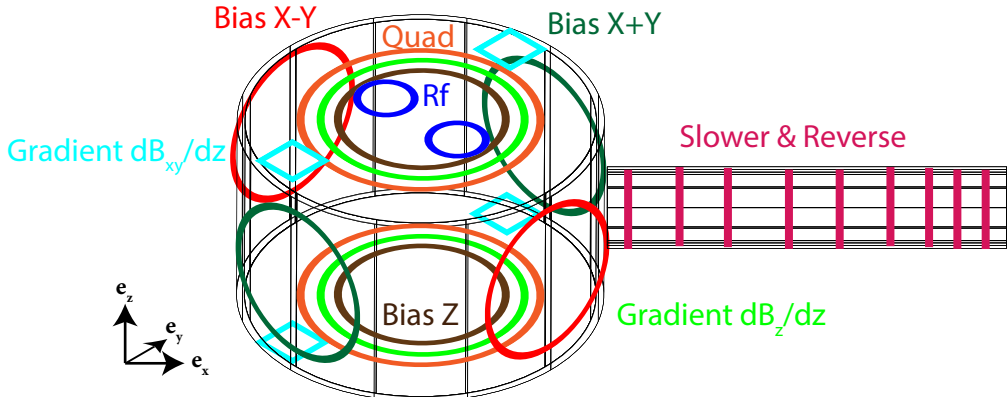


Figure 8: Schematic of magnetic coils on the RbK apparatus. The black wire frame represents the main experiment chamber, with the Zeeman slower off to the right. The Zeeman slower and reverse coils are wound around the Zeeman slower in varying spatial frequency (magenta). The quad (orange), gradient cancellation dB_z/dz (bright green) and bias Z (brown) are all pairs of identical coils on the top and bottom of the apparatus. Bias X-Y coils (red) are a pair of identical coils around the axes of the M_1 and M_3 mirrors, and the bias X+Y (dark green) are a pair of identical coils around the axes of the M_2 and M_4 mirrors. The rf coils (blue) are a pair of circular coils on top of the experimental chamber, spaced enough to allow the top MOT beam through. The gradient cancellation coils dB_{xy}/dz (cyan) are four square coils on top and bottom of the experiment along the X+Y axis.

^{40}K cooling and repump lasers are Toptica TA-pro systems, with the repump laser frequency stabilized to the ^{40}K atomic transition. In addition, a green plug beam (solid dark green in ??b) is used (see section ??), derived from a Coherent Verdi V-5 laser. For ^{40}K experiments detailed in Chapter ??, we used a near resonant retroreflected optical lattice beam, shown in dashed dark magenta entering past the M_4 flipper mirror, coming out past the M_2 mirror before getting retro-reflected.

3.3.2 Magnetic coils

Figure ?? is a schematic depiction of all the coils used to produce magnetic fields on the RbK apparatus. The quad coils (orange in the figure) are a large pair of coils used to produce a quadrupole field for the MOT. The top and bottom coils are connected through four IGBT switches, forming an h-bridge (see Figure 4.9 in [20]).

This allows switching between two configurations: anti-Helmholtz and Helmholtz. In anti-Helmholtz configuration, the top and bottom coils conduct current in opposite directions, producing a quadrupole field gradient at the center. This is the configuration used for the MOT, rf evaporation, and producing a Stern-Gerlach gradient for spin resolved imaging. In Helmholtz configuration, the two coils conduct current in the same direction, producing a strong bias field along the e_z direction. This was used to get close to the Feschbach resonance in the experiment detailed in Chapter ??.

There are three pairs of bias coils, used to cancel constant background fields or provide field offsets along the three axes. All three are in Helmholtz configuration. The bias Z coils (brown) are on top and bottom of the experiment and provide a constant B_z field at the center. The bias X+Y coils (dark green) are vertical on two opposite sides of the apparatus along the e_x+e_y directions, and the bias X-Y (red) are on the other two opposing sides along the e_x-e_y directions. There are also two sets of gradient cancellation coils available, although they are not subject to feedback loops or computer control. The first is another pair of coils on top and bottom of the apparatus (bright green), connected in anti-Helmholtz configuration to produce a small gradient dB_z/dz . The second is four square coils mounted above and below each bias X+Y coil (cyan). Both vertically stacked pairs of coils are wound in Helmholtz configuration, and the two pairs are in series, providing a small gradient dB_{xy}/dz at the atoms.

3.3.3 Procedure for making a BEC

We begin with the atoms heated in the ovens, sent through a thin nozzle allowing only those atoms with a velocity towards the science chamber to enter. They are cooled via a Zeeman slower and captured in a Magneto-Optical trap (MOT) in the science chamber. During this step, the Zeeman slower is on, with both the

coils and the slower cooling and repump lights on. These beams (dark blue in Figure ??b) are -148.5 MHz red detuned from the $|F = 2\rangle$ to $|F' = 3\rangle$ transition for cooling and -8.2 MHz red detuned from the $|F = 1\rangle$ to $|F' = 1\rangle$ transition for cooling (for this, the cooling TA is locked to a 133 MHz beat note offset from the master laser). At the same time, the flipper mirrors $M1 - 4, M_{bottom}, M_{top}$ are flipped in and the MOT cooling and repump beams (red in Figure ??) are on. The quad coils are on in anti-Helmholtz configuration with 25 A of current running through them, producing a field gradient of $\frac{dB_z}{dz} \approx 13$ Gauss/cm. This step can be set to take anywhere from ≈ 0.7 s to ≈ 5 s depending on how many atoms are needed.

Next is the optical molasses step, during which sub-Doppler cooling of the atoms occurs. For this step, the Zeeman coils and slower lights are turned off. The quad coil current is also switched off, leaving just the MOT cooling light and only leakage MOT repump light. The MOT cooling light is set to 20.6 MHz below the $|F = 2\rangle$ to $|F' = 3\rangle$ transition (120 MHz beat-note command). It is then linearly ramped in 19 ms down to a red detuning of 90.2 MHz (50 MHz beat-note command). Since the repump light is all but off in this step, the atoms are also depumped into the $F = 1$ manifold. Then, the atoms are optically pumped into the $|F = 1, m_F = -1\rangle$ state to make them trappable by the quadrupole field. This is done by turning on the slower repump beam (dashed dark blue in fig. ??b) 1 ms. Then, the XZ imaging beam (blue in fig. ??b) is briefly turned on to get rid of any remaining $F = 2$ atoms.

Next, we compress the atoms and perform forced rf evaporation. To compress, the quad coils are first turned on to 130 A. After holding for 20 ms, we sweep the current linearly to 250 A in 200 ms. The forced rf evaporation is then performed by turning on the rf coupling field and sweeping the frequency from 20 MHz to 4 MHz in 4 s to couple the highest energy atoms from $|F = 1, m_F = -1\rangle$ to $|F = 1, m_F = 0\rangle$ and allow them to escape the trap. The slow ramp is designed to allow the system

to rethermalize through collisions as the hottest atoms are ejected. During rf evaporation, the crossed optical dipole trap (ODT) is on at an initial command power of 2.0 V and initial split (command to AOM controlling the power split between the two crossing beams, shown in fig. ??b) of 0.01 V. This allows any atoms that are cold enough to see the optical trap to be captured by it.

Then, the atoms are decompressed and loaded into the ODT. The quad current is ramped down to 60 A exponentially with a time constant of $\tau = 1.5$ s in 3 s. This is the quad current at which the atoms are only barely suspended against gravity by the quadrupole trap. At the same time, the bias Z current is ramped down from 10 A to 8 A, lowering the center of the quadrupole trap to the ODT. Then, the atoms are further evaporated in the ODT. This is done over the course of 5 s, ramping down the depth of the ODT and allowing the hottest atoms to escape. During this step, the ODT power is ramped exponentially from the initial command of 2.0 V to a final command of 0.4 V, while the split command is ramped up linearly from 0.01 V to 0.65 V, effectively turning on the crossing -1^{st} order beam. It is during this evaporation step that the atoms are cooled below the critical temperature and Bose condense.

Finally, the quad current is ramped exponentially to 0 A in 5 s, leaving the atoms optically trapped. Then any desired experiment can be performed on the BEC. For daily checks of the BEC, no experiments are performed and the atoms are released from the trap and allowed to expand in time-of-flight for 16.2 ms before being absorption imaged in the XY plane by the PIXIS imaging camera, pictured in fig. ??b.

3.3.4 Changes to apparatus for Rubidium

In this section, we describe a few of the changes that were made to the apparatus since the writing of Lauren Aycock’s thesis [20]. This is not an exhaustive list,

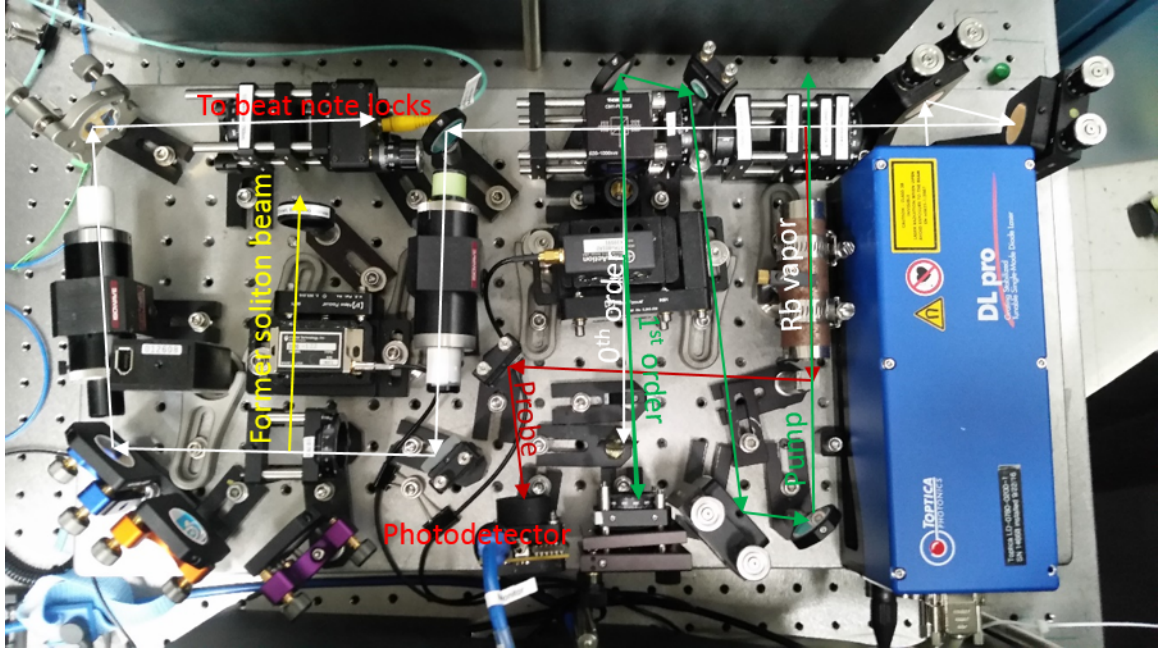


Figure 9: New master board layout.

but rather the most notable changes to the main setup affecting BEC production or adding capabilities to the apparatus.

3.3.4.1 Master laser setup

In 2014, the master laser board was replaced by a new version, with a new laser that was not dying. The laser was a Toptica DL-Pro, and it output approximately 80 mW, allowing for an extra beam arm that was used to imprint a phase shift on half the cloud to produce a soliton in the soliton project (see Appendix A) [21].

The layout of the new master laser board is shown in Figure ???. The board contains saturated absorption spectroscopy to lock the laser frequency relative to the atomic resonance, an output port to send to the cooling and repump lasers for beat note locking and monitoring purposes, and an ouput port (partially dismantled in the figure) for any use if necessary. There are two mirrors directly in at the laser output, for easy re-alignment of the whole board if a diode is changed or other internal laser adjustments are made.

After hitting the two mirrors, the beam is used for saturated absorption spectroscopy, as described in section 8.3 of [22]. It is first split into two branches by a polarizing beam splitter cube (PBS). The power split between the branches can be adjusted by a half waveplate (HWP) preceding the PBS. One branch is used as the probe beam in saturated absorption (red in the figure). This branch goes through the Rb vapor cell and is then sent to a photodetector. The photodetector reading is sent to a scope for monitoring and to a lock-in amplifier, used to derive the error signal for frequency locking. The rest of the beam (white) then hits another PBS cube (again preceded by a HWP to control the power split), splitting off the pump beam (green) for saturated absorption spectroscopy. This beam is sent to an acousto-optic modulator (AOM). This AOM's frequency is modulated by the lock-in amplifier, with modulation frequency of 100.0 kHz, amplitude of 0.356 V and phase shift (between the signal and photodetector response) of -115.44 degrees. The 0th order out of the AOM is blocked by a razor blade. The 1st order is retro-reflected in a cat's eye configuration [23]. Note that after retro-reflection, the second pass through the AOM also produces a 0th and 1st order beam. This 0th order beam is not blocked, but continues along the 1st order (pump beam) path at a slightly different angle - care must be taken to avoid aligning this order to counter-propagate with the probe. The double-passed beam (1st order in both directions, frequency shifted up twice) is then used as the pump and sent through the Rb vapor cell in the opposite direction of the probe beam.

The rest of the laser beam (white) then goes through an optical isolator, to avoid any subsequent reflections off of fiber tips or anything else from disturbing the saturated absorption frequency lock. Then, the beam hits another HWP followed by a PBS, splitting off the former soliton beam (yellow). In the figure, the soliton beam launch has been partially dismantled, but can be revived at any moment if needed. The beam was double-passed through an AOM in a cat's eye configuration

before being sent into a fiber launch. The rest of the laser power (white) is sent into a fiber that is connected to a fiber splitter box, providing light for beat note locking of the ^{87}Rb repump and cooling lasers as well as for monitoring the master laser on a wavemeter and Faby-Perot cavity.

3.3.4.2 Alignment imaging path

In 2016, there was a plan to carry out a project to create a 1D magnetic lattice whose topological character flips in the middle of the lattice, predicted to support localized states at the boundary. For this, two Raman beams needed to be overlapping, with one having a sharp phase change centered on the atoms. This required precise control of the beam phase as well as precise alignment of the beam center to the atoms. For optimal resolution, the Raman beams were to be sent upwards through the XY imaging system. To aid in alignment, it was decided that an additional imaging path that could detect these Raman beams directly be built. This alignment imaging path was implemented by Dr. Hsin-I Lu and is outlined in this section. All figures in this section were made by Hsin-I Lu.

The bottom part of the setup, with optics on the basement level of the experiment optical table, is diagrammed in Figure ???. One of the Raman beams, here called RamanC, first hit a spatial light modulator to imprint a phase jump. RamanC is then combined with a second beam, here called RamanD, on a PBS. Both overlapped beams are sent backwards through the XY imaging system and up towards the atoms. The dichroic filter allowed the Raman beams ($\lambda \approx 790$ nm) to be reflected while the imaging light ($\lambda \approx 780.24$ nm) passed through to the imaging cameras. The beam for alignment imaging is sent up to the atoms backwards along the XY imaging beam path. It entered the path via a mirror on a kinematic mount, which could be removed to allow imaging through the usual camera focused in situ in XY (see Figure ??).

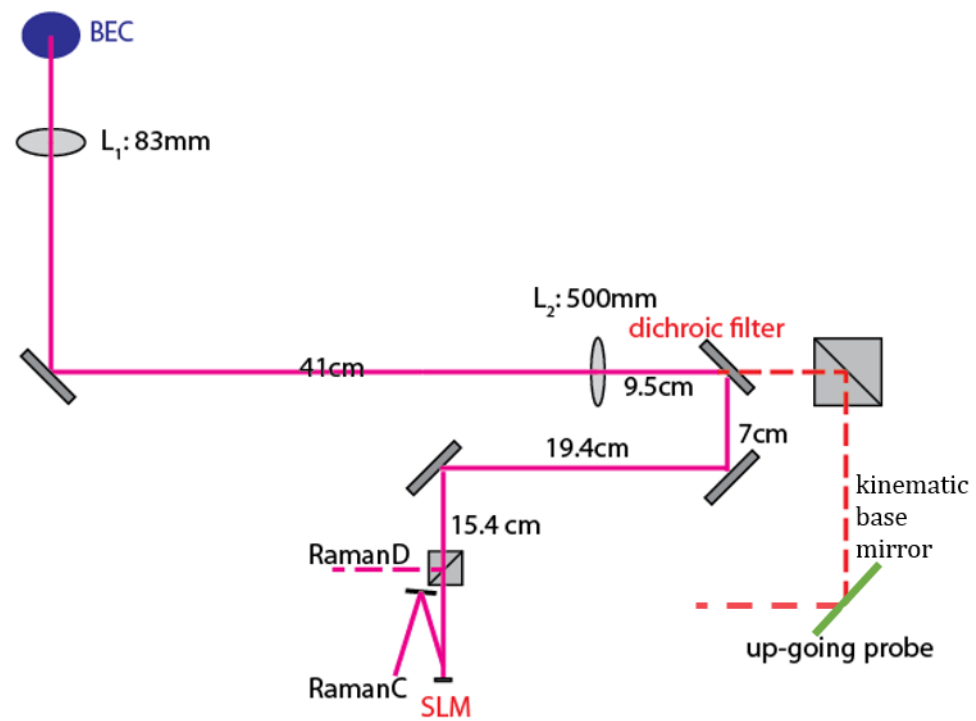


Figure 10: Schematic of the bottom half of the alignment imaging system, as well as the Raman beam set-up.

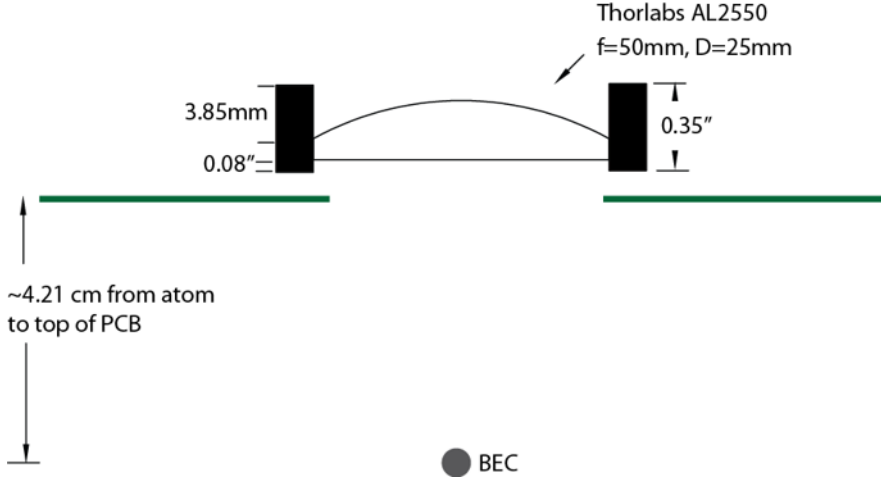


Figure 11: Schematic of the new imaging lens placed on the bucket window on top of the experimental chamber.

To set up an alignment imaging system going upwards through the chamber, it was necessary to insert a new imaging lens above the chamber, as close to the atoms as possible to maximize the numerical aperture. A schematic of this lens is shown in Figure ??, it is a 25 mm diameter $f = 50$ mm aspheric lens, a Thorlabs AL2550. This lens was placed above the printed circuit board (PCB) that contains the top bias Z coil and rf coils. It was held in a custom made mount.

The top part of the imaging system is diagrammed in Figure ???. Here, the alignment probe beam is light blue. From the atoms, the alignment probe beam hits the new imaging lens (labelled L_1). Then, if the top MOT mirror is flipped out, it hits another additional flipper mirror (here M_2) before reaching a second lens and hitting an additional Flea3 camera, on the 'balcony' level of the experiment. Since the imaging lens on top of the chamber cannot be taken in and out, it was necessary to correct the down-going probe beam and down-going MOT beam, ensuring they retain their size at the atoms. For the down-going probe beam, this was done by installing a telescope to expand the beam by a factor of 4 (L_6 and L_5 in the figure) and then add a lens (L_4 in the figure) that forms a telescope with the imaging lens to reduce the beam back down by a factor of 4. The MOT beam was corrected by

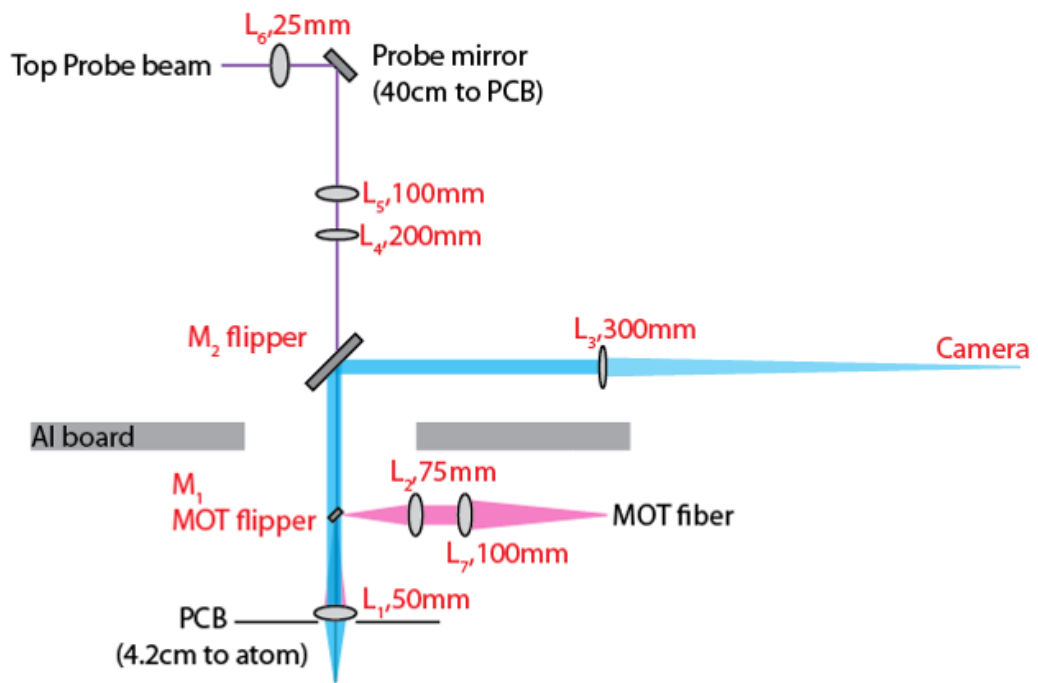


Figure 12: Schematic of the top half of the alignment imaging system, including correction optics for the MOT beam and probe beams to undo the effects of the new imaging lens.

switching the focusing lens directly after the MOT fiber to an $f = 100$ mm lens (L_7), effectively expanding the beam by a factor of $\approx 2/3$, and then adding an $f = 75$ mm lens (L_2) to form a telescope with the imaging lens, reducing the beam size by a factor of $2/3$. The adjusted beams were aligned and the experiment functioned properly. The alignment imaging system was also aligned with great effort.

3.3.4.3 FPGA quad servo

In 2014, the servo board that was used to stabilize the current in the quad coils had failed, and rather than replacing it with an identical one a new FPGA-based servo board design by Ryan Price was implemented. This design is described in detail in Appendix B of [24]. Here, we include a brief description of the design and implementation details for the quad servo at RbK.

The basic operation of the board is as follows. There are four SMA connections for input signals. These signals go to a 16 bit, 8 channel analog to digital converter ADAS3022BCPZ, then through a digital isolator Si8662BC-B-IS1, to the FPGA board. The outputs of the FPGA are sent through a similar digital isolator, Si8660BC-B-IS1 and into a 16 bit, 4 channel digital to analog converter AD5686R. Then, each of the four outputs is sent through a programmable gain amplifier AD8250ARMZ. The gain setting signal is derived from the FPGA board , by way of a serial shift register CD74HC4094. There are four SMA connections for outputs of each of the four amplifiers.

All of these devices are powered from a +/-18 supply voltage by way of three voltage regulators, LM2940C_KTT_3 for 5V regulation, LM2990_KTT_3 for -15V regulation, and LM2940CSX_KTT_3 for +15V regulation. The FPGA communication is set up through USB. There is a USB input port that connects to a USB chip FT232HL. The USB chip requires an EEPROM, in this case 93LC56BT is used. Clock timing for both the FPGA and the USB chip is provided by CTX292-LVCT.

There is also a buffer SN2564BCT25244 available for amplifying digital FPGA outputs. The digital side of the board is also powered from a separate 5V supply by way of a 3.3V regulator LM1085_KTT_3.

For quad coil current stabilization, the board receives a computer command, in volts, through one of it's input ports, and a Hall probe reading, in amps, through the other one. The Hall probe current sent to the servo is dropped across a stack of two 51 Ohm resistors (located inside the servo box) for a total measured resistance of 25 Ohms. The difference between the two inputs, in volts, is interpreted as the error signal by the FPGA board. The control output of the board is then sent to the gate input of a MOSFET bank. The power supply powering the quad coils is connected to this MOSFET bank and then to the coils in series. Controlling the gate voltage of the MOSFETs controls the resistance the power supply sees and thus the current it outputs (in voltage limited mode).

The optimal PID parameters, set via software and programed in the FPGA board, have been found at a gain factor of -5 and integrator bandwidth of 400 Hz. The resulting turn-on curve is shown in pink in Figure ?? a. For this curve, the computer command was hopped to 100 A and the resulting current as detected by the Hall probe was observed. The turn-on curve using the preceding servo board is shown in gray.

The board is also equipped with a digital TTL input (on the back of the board). When this digital input is high, the output control voltage is imediately railed to its lower bound. To be compatible with the MOSFETs used, the upper and lower bounds of the control output are set to 5 and 3 V respectively. The turn-off curve when this TTL switch is activated is shown in Figure ?? b. The timescale is likely limited by eddie currents in the chamber.

We calibrated the resulting current (as measured by the Hall probe) for different command voltages. This is shown in Figure ???. Both the schematic for the servo

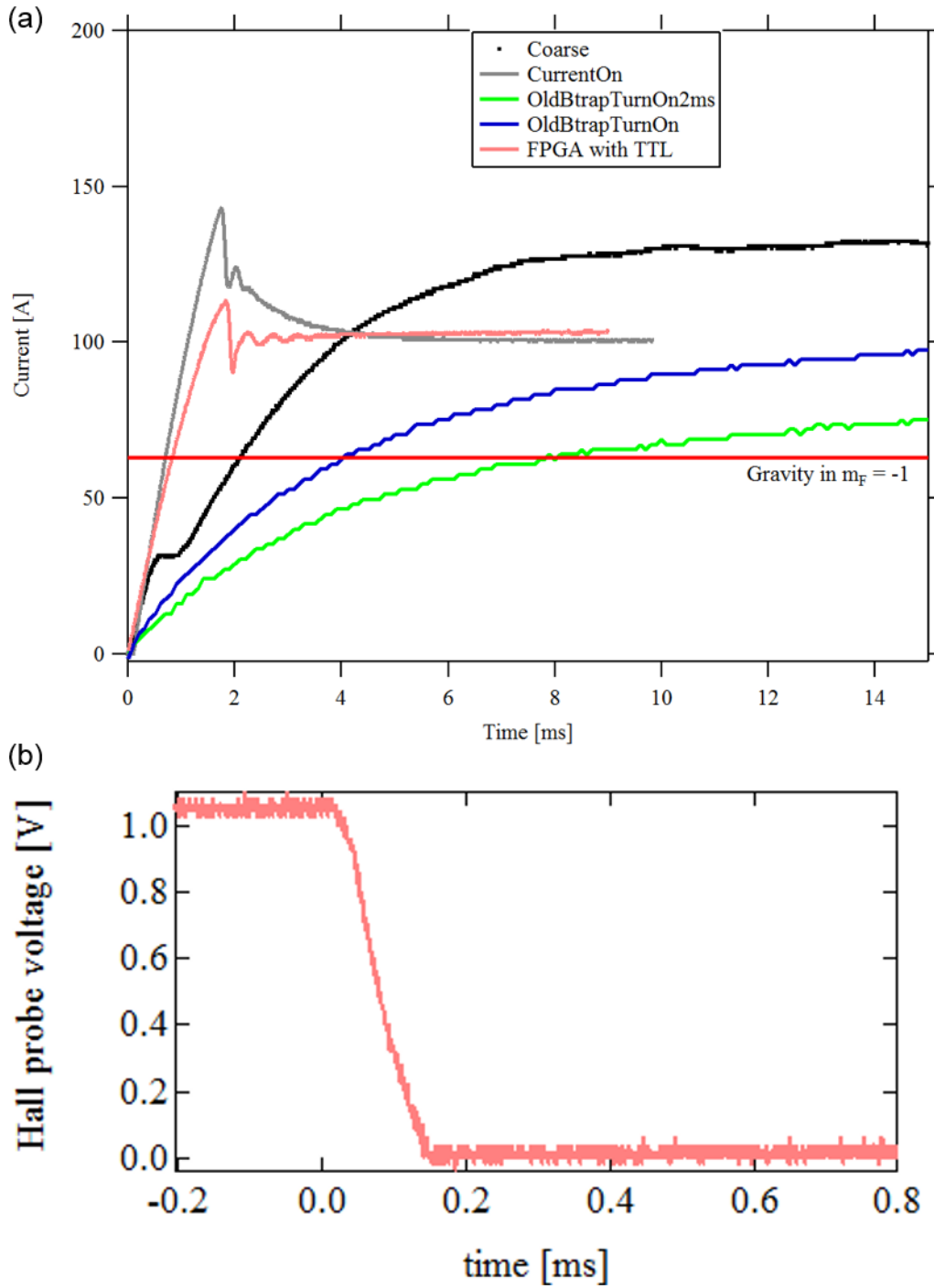


Figure 13: Turn on and off curves of the quad coils. (a) Turn-on, when computer command is jumped from 0 to 100 A . The FPGA-based servo response is in pink. The previous hardwired servo is in gray. The other curves are extraneous. (b). Turn-off with the FPGA-based servo when the TTL switch is engaged.

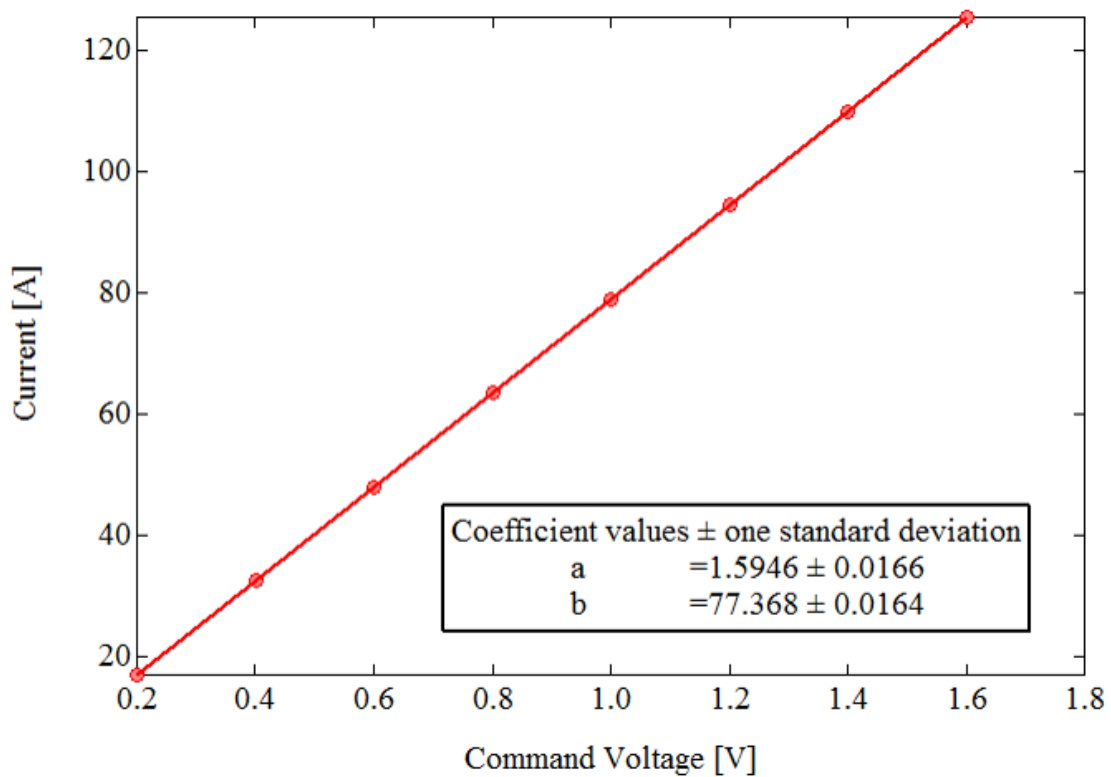


Figure 14: Output current as a function of computer command voltage for the FPGA-based servo implementation.

board and the Box control program to talk to the FPGA are in the shared google drive under 'RbK/Lab Notebook/Electronics/FPGA Quad Servo (From Ryan)'. When connected, the box control program detects 'RbK Quad Servo' in its device list. In the past, several cycles of plugging and unplugging as well as turning on and off have been necessary for the connection to be successfully made.

3.3.4.4 ODT beam shaping

In 2015, two projects were being carried out on the apparatus at the same time: the soliton project (see Appendix A) [21] and the synthetic dimensions project detailed in Chapter ???. The soliton project used an elongated BEC, requiring the dipole trap to be highly elongated along one direction, here $e_x + e_y$. For this, only the 0th order of the ODT was used and it was made very tight both along the horizontal and vertical directions: with 42 and 55 μm waists, respectively. The synthetic dimensions projects suffered from momentum changing collisions, and therefore needed the cloud to be as dilute as possible. For this, the 0th order ODT beam still needed to be tight in the vertical direction to suspend against gravity, but needed to be as wide as possible (while still retaining a detectable atom number) in the horizontal. Therefore, an extra cylindrical lens on a removable, rotatable mount was added in the beam path to switch between the two configurations.

The location of this new lens is detailed in Figure ???. Without this lens, the beam was sent through a telescope (the $f = -10$ and $f = 15$ cm lenses before reaching an $f = 25$ cm focusing lens, placed 25 cm away the center of the chamber to focus the beam at the atoms. The beam waist as a function of propagation distance along this beam path is shown in blue in Figure ?? a. This graph was made by Dr. Ian Spielman from a python calculation of Gaussian beam optics. According to the calculation, the beam is focused down to a 45 μm waist at the atoms located at a displacement of 1400 mm.

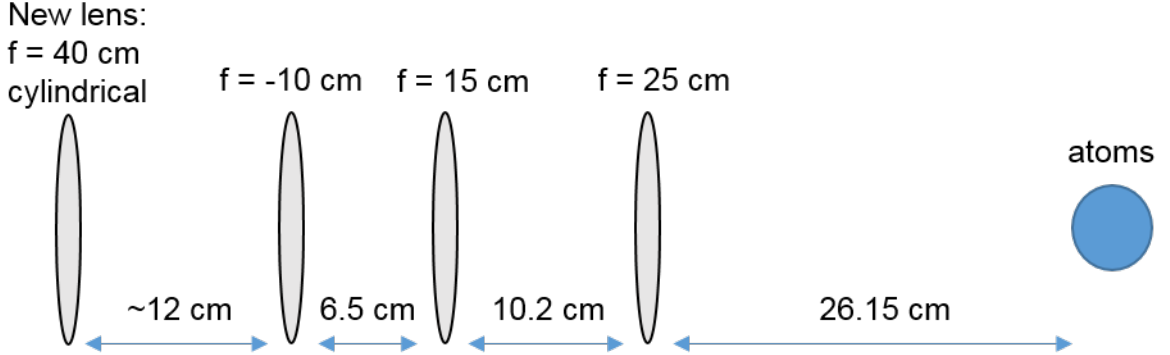


Figure 15: Schematic of beam shaping optics in the path of the 0th order ODT beam, after the split AOM. The new lens, on a removable mount, is cylindrical, shaping the beam along the horizontal axis only.

The additional lens used was an $f = 40$ cm cylindrical lens, rotated in its rotating mount to focus the beam slightly in the horizontal direction. The effect of this lens on the horizontal beam waist along its path was calculated and plotted (again by Ian using his code) in Figure ?? b. This plot was made for a $f = 75$ cm lens instead of $f = 40$ cm, but the qualitative effect is the same. As seen in the figure, the waist of the beam is not significantly impacted by the addition of the lens, but the focus is shifted away from the atoms, resulting in a larger waist at the atoms. The horizontal beam waist at the atoms with the $f = 40$ cm lens as measured by a beam profiler camera was $115 \mu\text{m}$. This was the configuration used in the experiments described in Chapter ??.

3.3.5 Procedure for making a DFG

To make a degenerate Fermi gas of ${}^{40}\text{K}$, we followed a similar cooling procedure as for making a BEC, with some key differences. First, as mentioned in sec. ??, due to the Pauli exclusion principle, spin polarized ${}^{40}\text{K}$ atoms cannot undergo s -wave collisions, and therefore below a certain temperature have no method to thermalize on their own and cannot be evaporatively cooled. To overcome this problem, we cooled a mixture of ${}^{87}\text{Rb}$ and ${}^{40}\text{K}$, effectively using ${}^{87}\text{Rb}$ as a collisional bath to allow

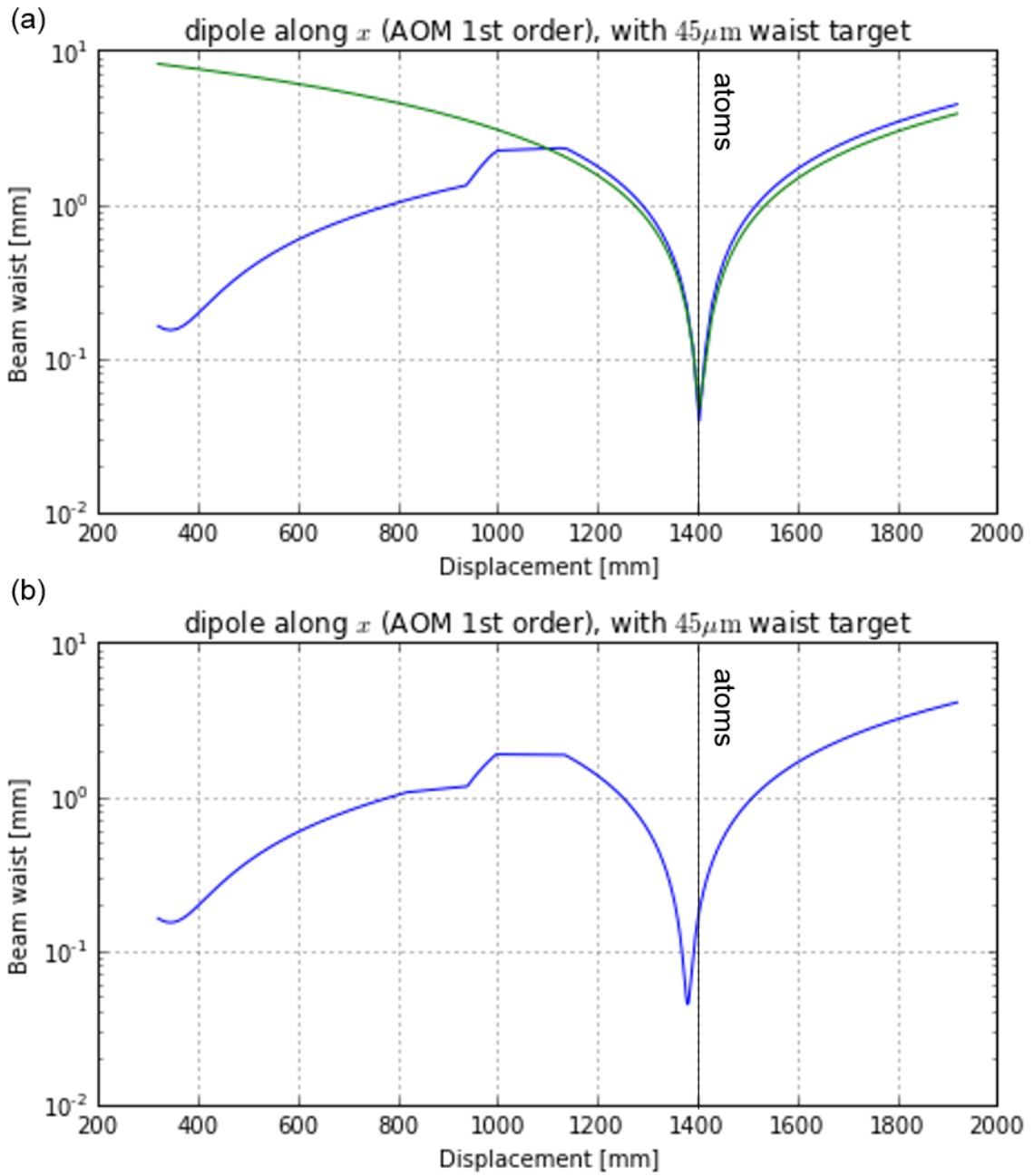


Figure 16: Beam waist as a function of propagation distance as calculated by Ian Spielman's code. Graphs also made by Ian Spielman. The atoms are at displacement = 140 cm. (a) Without additional lens. Blue line represents horizontal beam waist. (b) With an additional $f = 75$ cm lens 12 cm in before the next optic.

the Fermions to thermalize. Second, ^{40}K is slightly below half the mass of ^{87}Rb . This leads to a larger magnitude of transverse velocity for ^{40}K atoms in the Zeeman slower, leading to a larger fraction of atoms missing the capture region of the MOT. To mitigate this issue, we utilized transverse cooling of ^{40}K right before the Zeeman slower. This consisted of two pairs of counter-propagating beams along the $e_z + e_y$ and $e_z - e_y$ directions, performing Doppler cooling in the directions perpendicular to propagation (not shown in fig. ??b). The lower mass of ^{40}K , as well as the larger number of available spin states, also leads to a larger number of Majorana losses near the center of the MOT: spin flips that take the atoms out of the trappable states because they are moving too fast to adiabatically follow the changing magnetic field direction [25–27]. To mitigate this issue, for cooling ^{40}K the center of the quadrupole trap was plugged by a tightly focused green (repulsive) laser beam (dark green in fig. ??b).

First, ^{40}K atoms starting at the oven were cooled via a Zeeman slower and transverse cooling and captured in a MOT for 7 s. Then, both ^{40}K and ^{87}Rb atoms were slowed and MOT loaded for 1.5 s. The subsequent optical molasses step was only 2 ms long, with the ^{87}Rb MOT cooling light ramped linearly from 20.6 MHz below the the $|F = 2, m_F = 2\rangle$ to $|F = 3, m_F = 3\rangle$ transition (120 MHz beat-note command) to 40.6 MHz below the resonance (100 MHz beat-note command). In this time, the ^{40}K cooling light was turned down in intensity but the detuning remained unaltered.

Next, ^{87}Rb was optically pumped into the $|F = 2, m_F = 2\rangle$ state using the slower cooling beam, while ^{40}K was optically pumped into the $|F = 9/2, m_F = 9/2\rangle$ state using a dedicated optical pumping beam in $250\mu\text{s}$. These are magnetically trappable states, and we subsequently turned on the quad coil current to 130 A to capture the atoms in the magnetic trap, along with the green plug beam at the center to prevent Majorana losses. Both species were compressed by a linear ramp

of the quad current up to 160 A in 0.5 s. Then, forced rf evaporation was performed for 10 s, sweeping the rf frequency linearly from 18 MHz down to 2 MHz.

Then, the atoms were decompressed and loaded into the ODT, similarly to the BEC procedure. The ODT was turned on to an initial power of 2 V and an initial split command of 0.01 V. The quad current was ramped down to 25.5 A exponentially with a time constant of $\tau = 1.5$ s in 3 s. The evaporation in the ODT was split into two steps. During the first 3 s step, the split was ramped linearly to its final command power of 0.65 V, putting more power into the (less tightly focused) crossing beam. The green plug beam was ramped off during this step. During the second, 4 s step, the overall power of the ODT was exponentially ramped down to 1.2 V, while the quad coil current was ramped exponentially to 0 A.

We then used adiabatic rapid passage (ARP, see sec. 2.2.3) to transfer the ^{87}Rb atoms from $|F = 2, m_F = 2\rangle$ to $|F = 1, m_F = +1\rangle$ using a microwave coupling field and a 50 ms ramp in bias Z coil current. Then, we pulsed on the XZ imaging beam to eject any remaining $F = 1$ atoms. Then we performed one last evaporation step in the ODT, ramping the final power down to 0.7 V. The ^{87}Rb atoms were no longer suspended against gravity and fell out of the trap. We then were free to perform experiments with the degenerate ^{40}K cloud.

3.3.6 Current status of Potassium apparatus

At the time of writing, the ^{40}K part of the apparatus as described is no longer functional. The number of ^{40}K atoms collected in the MOT started decaying significantly in January 2014, and by March was almost completely gone and could not be resurrected. The specific failure point of the setup was not clear. However, other groups have found that atomic sources are much more stable, and a higher fraction of the (expensive) ^{40}K sources can be utilized when the atoms were initially cooled with a 2-D MOT rather than with a Zeeman slower [28–30]. Therefore, rather than

continuing to attempt to revive the existing set-up, the decision was made to build a 2-D MOT for both ^{40}K and ^{87}Rb .

The design of our 2D MOT is closely based on the design in Thomas Uehlinger's diplome thesis [29]. The design was developed by Dalia Ornelas, and initially implemented by Marcell Gall before it was taken over by the rest of the RbK team. The schemtaic of the planned vacuum system (with attached optics) is pictured in Figure ???. On the left side of the schematic, there are optics directing the pushing beam into a miniconflat viewport. The viewport is part of a cross, with the ^{40}K and ^{87}Rb ovens attached to the two ends of the cross, with gate valves allowing one to close off one or both sources from the rest of the vacuum system. From there, the cross attaches to the main 2D MOT cell via a mini-conflat flange.

The cell is a custom machined stainless steel frame with rectangular anti-reflection (AR) coated windows on four sides and mini-conflat conectors on two ends, pictured in more detail in Figure ???. Two aluminum mounting crosses attach two either end of the cell. Four aluminum bars are connected between the crosses, and the main 2D MOT optics are mounted on those four bars. The opposite end of the cell (right in fig. ???) sandwiches a differential pumping tube in the mini-conflat connection and connects to another cross. The top of the cross connects to a small ion pump. The bottom connects to a rotatable feed-through mechanism with a 'flag', a square of metal, attached inside. The rotator rotates the flag in and out of the atomic beam path, providing a means of losing off the main chamber from the atomic beam and push beam light. The fourth end of the cross connects to another gate valve, separating the 2D MOT vacuum system from the main experiment chamber. The other end of this gave valve connects to a flange that is meant to connect directly to the main experiment chamber.

A picture of the stainless cell is shown in Figure ???. Attaching the glass windows to the stainless steel frame in a vacuum tight way proved to be quite

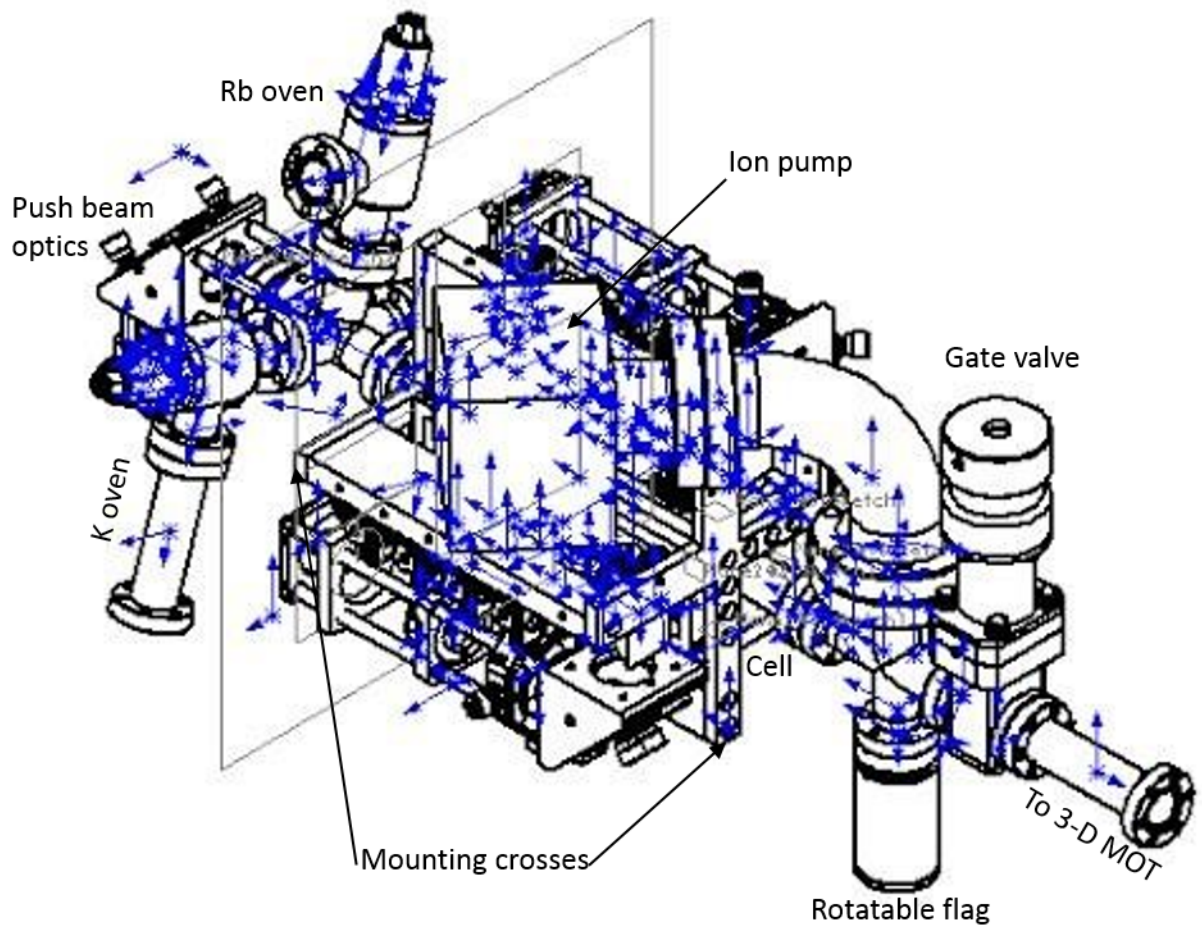


Figure 17: Schematic of the 2D MOT setup. The mini-conflat on the right is to be attached to the existing experiment chamber, directing the atomic beam into the 3D MOT.

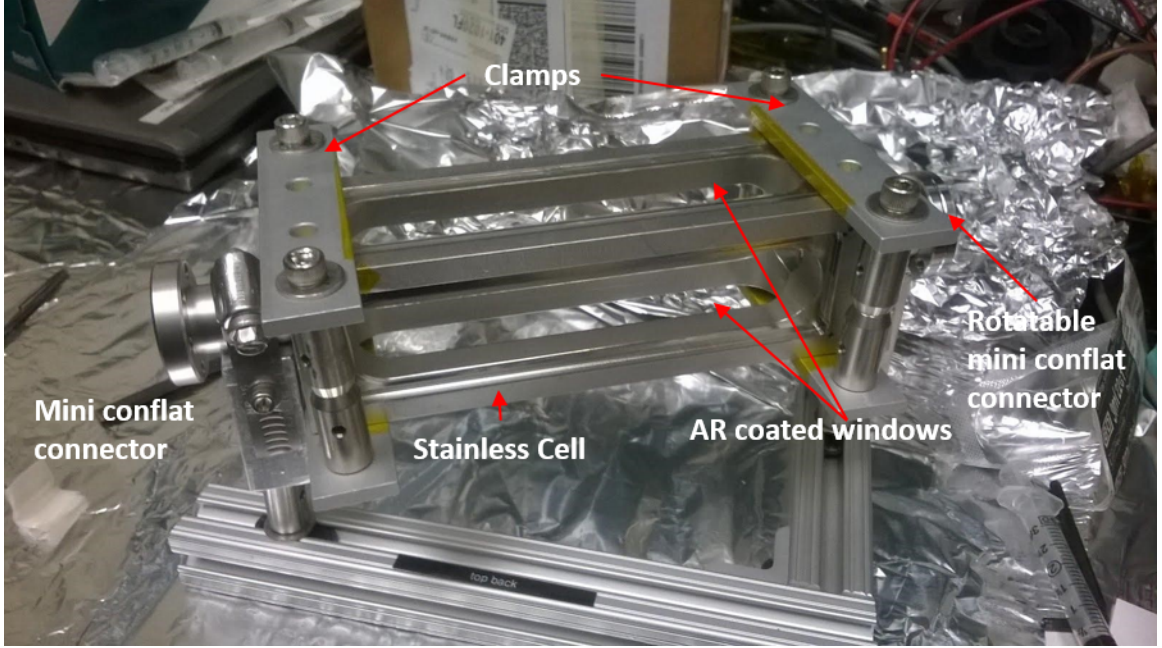


Figure 18: Picture of 2D MOT cell during an attempt to epoxy AR coated windows onto the stainless steel frame. The clamps serve to hold the windows in place while epoxy cures.

difficult, and this picture was taken during one of the attempts to do so using epoxy. The clamps around the cell served to keep the windows in place as the epoxy was curing. In the final design, the seal was made with indium, with gaskets custom machined to press the windows onto the cell. We roughly followed the indium sealing method presented in [31], with gaskets above and below the windows. We also employed pre-squashing, where a metal piece in the shape of the window was first pressed onto the indium wire to flatten it and minimize the amount of pressure that needed to be applied to the glass window.

The main 2D MOT optics direct the cooling and repump beams into the cell from two directions, and retro-reflect them on the other end, producing cooling along those two directions (hence the name 2D MOT). The optical set-up along one of those directions is presented schematically in Figure ???. The cell is elongated along the atomic beam direction, to maximize the time the atoms are cooled while travelling to the 3D MOT. Because of this, instead of a highly elliptical cooling beam,

four MOT beams are launched in a row, almost overlapping, from each of the two directions. This is accomplished by splitting one beam into four with four sequential beam-splitting cubes (BSs).

The 2D MOT cooling and repump light is first periscoped over from a fiber and lens assembly (designed to shape the beam to be roughly 1 inch in diameter). It then goes through a half-wave plate (HWP) before entering the first 70/30 beam splitter. 30% of the light is sent through a quarter-wave plate (QWP) tuned to provide circularly polarized light into the cell. On the other side of the cell, the beam hits another QWP before being retro-reflected back into the cell. Since the beam hits the QWP on the other side of the cell twice, the circular polarization is preserved. The remaining 70% of the light goes into the next 70/30 BS, sending 21% of the total beam power into the second arm going into the cell, to be retro-reflected in the same way. The remaining 49% hits a 50/50 BS, sending 25.5% of the total beam power into the third retro-reflected arm. The final cube is a polarizing beam-splitter (PBS), and the HWP before the cubes is tuned to ensure all of the light is sent into the cell on this last, fourth, arm.

The push beam enters from the oven direction and serves to provide some velocity to the atoms along the long direction of the cell to ensure they continue to travel to the 3D MOT, while still providing some cooling along the longitudinal direction. In order to provide this cooling, the push beam is also retro-reflected, with the help of a custom machined differential pumping tube (on the right in fig. ??). The differential pumping tube is machined to have a 45° angled polished end, reflecting all of the light except for the central part towards a retro-reflecting mirror outside the cell. Along the other 2D-MOT cooling direction (up and down in fig. ??), this whole set of optics is replicated, with the exception of the push beam retro-reflection.

The current 2D-MOT setup is pictured in Figure ???. The vacuum system has

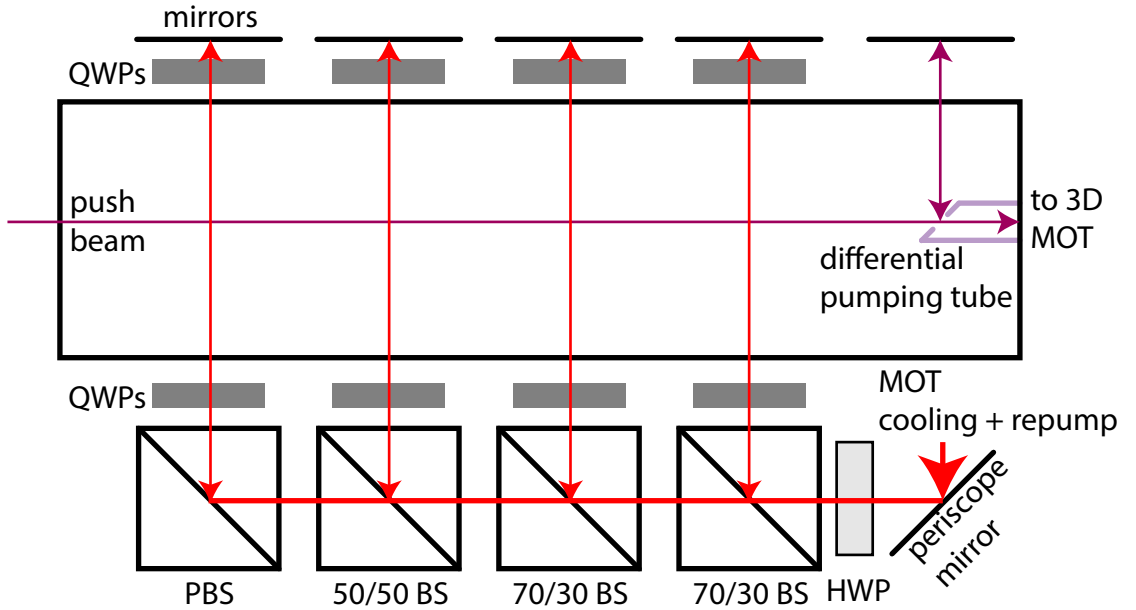


Figure 19: Schematic of 2D MOT optics along one direction. The main cooling and repump beam is split into four parallel arms by four beam splitter cubes. The push beam enters from the oven direction and is retro-reflected via a custom machined and polished differential pumping tube. These optics are mounted on crosses attached to the 2D MOT cell.

been assembled and successfully pumped down, with a octagonal test chamber in place of the main experimental chamber. This test chamber is intended to be used to send probe light through and detect fluorescence to characterize the atomic beam coming out of the 2D MOT. The optics have been assembled and the quarter-wave plates lightly epoxied onto the BS cubes and mirrors, although as can be seen in the picture some have regrettably fallen off. Quadropole coils have been wound around each of the four windows, onto 3D printed coil winding forms. Bias Z coils have also been wound to cancel out stray gradients along the atomic beam direction.

The two Toptica TA-pro systems that were used to provide all ^{40}K light in the past are still operational, and need to be re-purposed to provide both 2D MOT and 3D MOT cooling and repump light. A new Toptica TA-pro was also purchased, with the intent to implement gray molasses cooling on the ^{40}K D1 line as described in [32].

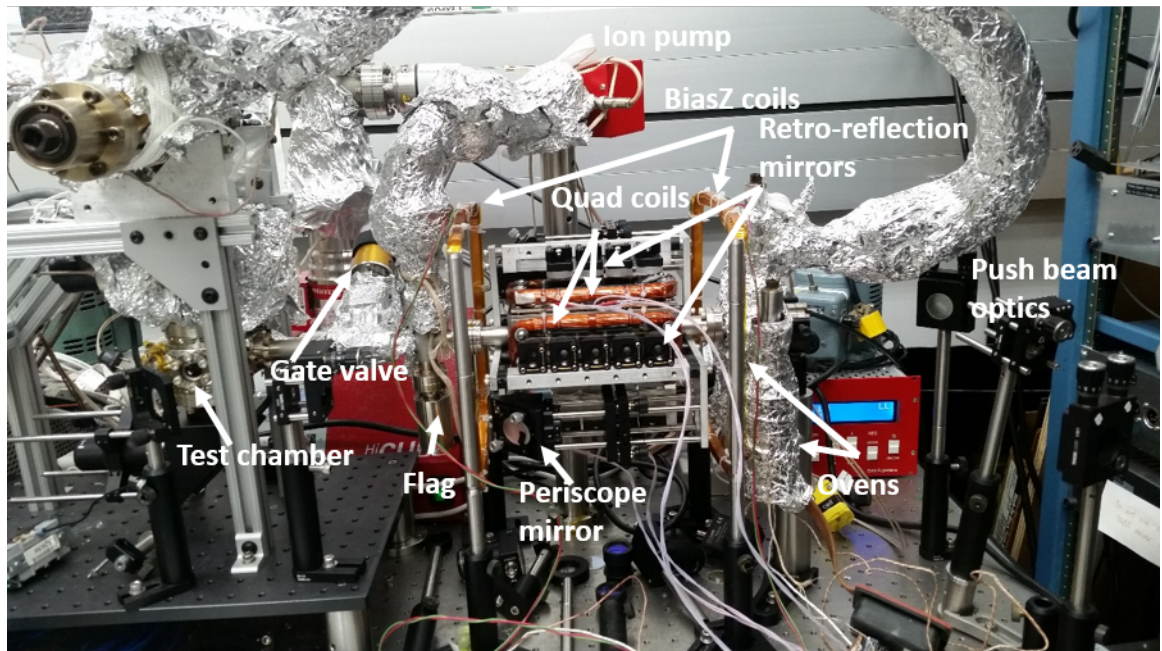


Figure 20: Picture of current 2D MOT apparatus. The vacuum system is in place, optics are (mostly) mounted and coils to generate the quadrupole trap and cancel gradients along the atomic beam direction have been wound.

Bibliography

- [1] J. R. Ensher, D. S. Jin, M. R. Matthews, C. E. Wieman, and E. A. Cornell. Bose-einstein condensation in a dilute gas: Measurement of energy and ground-state occupation. *Phys. Rev. Lett.*, 77:4984–4987, Dec 1996.
- [2] C.J. Pethick and H. Smith. *Bose-Einstein Condensation of Dilute Gases*. Oxford University Press, Oxford, UK, 2005.
- [3] M. Egorov, B. Opanchuk, P. Drummond, B. V. Hall, P. Hannaford, and A. I. Sidorov. Measurement of *s*-wave scattering lengths in a two-component bose-einstein condensate. *Phys. Rev. A*, 87:053614, May 2013.
- [4] W. Ketterle and M. W. Zwierlein. Making, probing and understanding ultracold Fermi gases. In *Ultracold Fermi Gases, Proceedings of the International School of Physics ‘Enrico Fermi’, Course CLXIV*, Varenna, 20-30 June 2006.
- [5] K. M. O’Hara, S. L. Hemmer, M. E. Gehm, S. R. Granade, and J. E. Thomas. Observation of a strongly interacting degenerate Fermi gas of atoms. *Science*, 298(5601):2179–2182, 2002.

- [6] S. Jochim, M. Bartenstein, G. Hendl, J. Hecker Denschlag, R. Grimm, A. Mosk, and M. Weidemüller. Magnetic field control of elastic scattering in a cold gas of fermionic lithium atoms. *Phys. Rev. Lett.*, 89:273202, Dec 2002.
- [7] K. Dieckmann, C. A. Stan, S. Gupta, Z. Hadzibabic, C. H. Schunck, and W. Ketterle. Decay of an ultracold fermionic lithium gas near a feshbach resonance. *Phys. Rev. Lett.*, 89:203201, Oct 2002.
- [8] T. Loftus, C. A. Regal, C. Ticknor, J. L. Bohn, and D. S. Jin. Resonant control of elastic collisions in an optically trapped fermi gas of atoms. *Phys. Rev. Lett.*, 88:173201, Apr 2002.
- [9] C. A. Regal, C. Ticknor, J. L. Bohn, and D. S. Jin. Tuning p -wave interactions in an ultracold fermi gas of atoms. *Phys. Rev. Lett.*, 90:053201, Feb 2003.
- [10] C. Chin, R. Grimm, P. Julienne, and E. Tiesinga. Feshbach resonances in ultracold gases. *Rev. Mod. Phys.*, 82:1225–1286, 2010.
- [11] M. Greiner, C. A. Regal, and D. S. Jin. Emergence of a molecular Bose-Einstein condensate from a Fermi gas. *Nature*, 426(6966):537–540, 2003.
- [12] M. W. Zwierlein, C. A. Stan, C. H. Schunck, S. M. F. Raupach, S. Gupta, Z. Hadzibabic, and W. Ketterle. Observation of Bose-Einstein condensation of molecules. *Phys. Rev. Lett.*, 91:250401, 2003.
- [13] S. Jochim, M. Bartenstein, A. Altmeyer, G. Hendl, S. Riedl, C. Chin, J. Hecker Denschlag, and R. Grimm. Bose-Einstein condensation of molecules. *Science*, 302(5653):2101–2103, 2003.
- [14] M. Bartenstein, A. Altmeyer, S. Riedl, S. Jochim, C. Chin, J. Hecker Denschlag, and R. Grimm. Collective excitations of a degenerate gas at the bec-bcs crossover. *Phys. Rev. Lett.*, 92:203201, 2004.

- [15] T. Bourdel, L. Khaykovich, J. Cubizolles, J. Zhang, F. Chevy, M. Teichmann, L. Tarruell, S. J. J. M. F. Kokkelmans, and C. Salomon. Experimental Study of the BEC-BCS Crossover Region in Lithium 6. *Phys. Rev. Lett.*, 93:050401, 2004.
- [16] M. W. Zwierlein, C. A. Stan, C. H. Schunck, S. M. F. Raupach, A. J. Kerman, and W. Ketterle. Condensation of pairs of Fermionic atoms near a Feshbach resonance. *Phys. Rev. Lett.*, 92:120403, 2004.
- [17] C. A. Regal, M. Greiner, and D. S. Jin. Observation of resonance condensation of fermionic atom pairs. *Phys. Rev. Lett.*, 92(4), 2004.
- [18] Y.-J. Lin, A. R. Perry, R. L. Compton, I. B. Spielman, and J. V. Porto. Rapid production of ^{87}Rb bose-einstein condensates in a combined magnetic and optical potential. *Phys. Rev. A*, 79:063631, Jun 2009.
- [19] Karina Jimenez-Garcia. *Artificial Gauge Fields for Ultracold Neutral Atoms*. PhD thesis, Joint Quantum Institute, National Institute of Standards and Technology, and the University of Maryland, 2012.
- [20] Lauren M. Aycock. *Topological excitations in a Bose gas and sexual harassment reported by undergraduate physicists*. PhD thesis, Cornell University, Ithaca, NY, 1 2017.
- [21] Lauren M. Aycock, Hilary M. Hurst, Dmitry K. Efimkin, Dina Genkina, Hsin-I Lu, Victor M. Galitski, and I. B. Spielman. Brownian motion of solitons in a bose-einstein condensate. *Proceedings of the National Academy of Sciences*, 114(10):2503–2508, 2017.
- [22] Christopher J. Foot. *Atomic Physics*. Cambridge University Press, Cambridge, UK, 2002.

- [23] E. A. Donley, T. P. Heavner, F. Levi, M. O. Tataw, and S. R. Jefferts. Double-pass acousto-optic modulator system. *Review of Scientific Instruments*, 76(6):063112, 2005.
- [24] Ryan Price. *Phase transitions in engineered ultracold quantum systems*. PhD thesis, University of Maryland College Park, Digital Repository at the University of Maryland, 6 2016.
- [25] E. Majorana. Atomi orientati in campo magnetico variabile. *Nuovo Cimento*, 9:43–50, Feb 1932.
- [26] C. V. Sukumar and D. M. Brink. Spin-flip transitions in a magnetic trap. *Phys. Rev. A*, 56:2451–2454, Sep 1997.
- [27] D. M. Brink and C. V. Sukumar. Majorana spin-flip transitions in a magnetic trap. *Phys. Rev. A*, 74:035401, Sep 2006.
- [28] J. Catani, P. Maioli, L. De Sarlo, F. Minardi, and M. Inguscio. Intense slow beams of bosonic potassium isotopes. *Phys. Rev. A*, 73:033415, Mar 2006.
- [29] Thomas Uehlinger. A 2-d magneto-optical trap as a high flux source of cold potassium atoms. Master’s thesis, Swiss Federal Institute of Technology Zurich, Zurich, 5 2008.
- [30] E. Pedrozo-Peafiel, F. Vivanco, P. Castilho, R. R. Paiva, K. M. Farias, and V. S. Bagnato. Direct comparison between a two-dimensional magneto-optical trap and a zeeman slower as sources of cold sodium atoms. *Laser Physics Letters*, 13:065501, May 2016.
- [31] K. J. Weatherill, J. D. Pritchard, P. F. Griffin, U. Dammalapati, C. S. Adams, and E. Riis. A versatile and reliably reusable ultrahigh vacuum viewport. *Review of Scientific Instruments*, 80(2):026105, 2009.

- [32] D. Rio Fernandes, F. Sievers, N. Kretzschmar, S. Wu, C Salomon, and F. Chevy. Sub-doppler laser cooling of fermionic 40k atoms in three-dimensional gray optical molasses. *Europhysics Letters*, 100:63001, Dec 2012.